Distributed dispense of operating liquid on rotating substrates in wet processing facilities

Diploma thesis

B. Dunkl

December 18, 2012

Supervisor: Ao. Univ.-Prof. Dipl.-Ing. Dr. techn. H. Steiner

Deutsche Fassung:
Beschluss der Curricula-Kommission für Bachelor-, Master- und Diplomstudien vom 10.11.2008
Genehmigung des Senates am 1.12.2008

EIDESSTATTLICHE ERKLÄRUNG

Ich erkläre an Eides statt, dass ich die vorliegende Arbeit selbstständig verfasst, andere als die angegebenen Quellen/Hilfsmittel nicht benutzt, und die den benutzten Quellen wörtlich und inhaltlich entnommene Stellen als solche kenntlich gemacht habe.

Graz, am ……. ……..
(Unterschrift)

Englische Fassung:

STATUTORY DECLARATION

I declare that I have authored this thesis independently, that I have not used other than the declared sources / resources, and that I have explicitly marked all material which has been quoted either literally or by content from the used sources.

……. ……..
date (signature)

Acknowledgment

The present work was produced at the Institute of Fuild Mechanics and Heat transfer at Graz Univeristy of Technology in cooperation with Lam Research in Villach. I want to thank Dr. Staudegger from Lam Reseach for the ideas and the support he gave and Prof. Brenn, Prof. Steiner and others from the Institute of Fluid Mechanics and Heat Transfer who where always helpful when I was looking for advise.

Abstract

The dispense of a working fluid on a rotating substrate is a key technology in the production process of microelectronic devices. The present work investigates two new dispenser designs for this purpose, a multi-hole dispenser and a narrow slot dispenser, both equipped with the same straight rectangular distribution channel. The layouts of the exits of these two dispenser types were designed to provide a most uniform outflow distribution along the length of the dispenser. The flow through the considered dispenser types is computationally investigated with two alternative concepts, three-dimensional CFD simulation, and a one-dimensional model approach based on the stream-tube theory. The computationally less costly one-dimensional model captures the main features of the flow inside the manifold fairly well. Strong deviations from the results of the three-dimensional CFD simulation mainly appear in regions, where the flow is dominated by three-dimensional phenomena, which are beyond the scope of the one-dimensional model. It is further shown that at the lowest investigated volumetric flow rates the transition from continuous exit jet flow to a discontinuous dripping has to be expected.

Contents

1. Introduction

In the semiconductor industry the production process of microelectronic devices involves various cleaning, cleansing and etching substeps, where a working fluid is dispensed on a substrate, the so called wafer. There exist several methods for wetting the wafer. One method is to rotate the wafer and supply the fluid by a single vertical jet moving across the disk. The steady drive to increase the production rate of microelectronic devices strongly motivates to extend the wafers in size. However, larger wafer sizes make it more difficult to ensure the required wetting of the surface using a single-jet dispenser. This led to the idea of supplying the fluid via multiple jets or via a thin liquid sheet. The computational investigation of the flow through a dispenser, where the liquid exits as multiple jets through a multi-hole nozzle, or, alternatively as a continuous liquid sheet, through a narrow slot are subject of the present work. For this purpose a simplified analytical approach as well as a more comprehensive numerical concept based on CFD[1] are proposed, which both can be used to calculate the flow rates of the liquid jets through the individual exit holes of the multi-hole dispenser, or, the continuous exit velocity variation along a thin liquid sheet, when considering a narrow slot dispenser. The computational investigation considers in particular a dispenser design, whose geometrical shape and size, inflow and outflow conditions are orientated on the real technical application. The commercial software Ansys-Fluent is used for the CFD simulation. For the simplified analytical approach an adequate computational solution algorithm is developed and programmed in Matlab. The development and testing of the computational tool, which is intended to give a reduced but still reliable description, represents an important part of this work. In section 3 two different dispenser designs are examined. For the first considered design the flow through a seven-hole nozzle is calculated using the analytical approach and the CFD concept. For the second considered design the flow distribution generated with a slot dispenser is investigated analytically. Computational tools have been developed for the analytical calculations of the flow through the dispenser. The tools are described in detail in appendix A.

1.1. Objectives

For a first estimation of the performance of a certain nozzle design using a multi-hole or narrow slot orifice, a quick estimation of the expected variation of the outflow rate along the manifold is needed. Therefore, an efficient computational tool has to be developed, which represents an appropriate alternative to computationally expensive CFD simulations. The scope of this efficient computational tool shall be assessed by a using the CFD approach. Therefore, the CFD has to give a detailed, reliable description of the flow inside the dispenser. Furthermore, a three-dimensional CFD simulation shall reveal the effect of the position of the dispenser inlet on the outflow rate variation. Finally, a criterion shall be formulated to ensure a continuous stable jet exit flow at the individual outlet ports of the dispenser, without a capillary brakeup of the

[1] CFD abbreviates “Computational Fluid Dynamics”

jets right after leaving the dispenser, to avoid the operation of the dispenser in a discontinuous dripping mode.

1.2. Literature review

One of the first works investigating the distributed dispense of fluid through manifolds for use in wet process facilities was carried out by Senecal [7]. He stated that the flow distributing behavior of a dispenser is mainly dependent on:

- the kinetic energy and the streamwise momentum of the main stream inside the distributor channel, and
- the frictional loss in the distributor.

Beside these two main influences, there exist further ones, which have a significant effect on the outflow behavior. One of these, mentioned by Senecal [7], are the upstream flow conditions. Senecal [7] gave a schematic overview, how kinetic energy and momentum, frictional loss and upstream flow conditions affect the outflow distribution in case of a perforated pipe dispenser. Thereby, Senecal [7] distinguished four different basic types of outflow distributions along the pipe as shown in figure 1.1:

1. Uniform distribution. This is the case, if the kinetic energy of the fluid and the frictional forces in the pipe are in a proper balance (figure 1.1a).
2. Rising outflow rate from the inlet to the end. The streamwise increase in static pressure caused by the loss of the kinetic energy due to the exiting fluid predominates over the pressure drop due to frictional losses along the pipe (figure 1.1b).
3. Falling outflow rate from the inlet to the end. The static pressure drop due to frictional losses predominates over increase in static pressure associated with the reduction of the kinetic energy of the fluid along the pipe (figure 1.1c).
4. Falling outflow rate near the inlet and rising outflow rate towards the end. In this case the effect of the streamwise decrease of the kinetic energy of the fluid basically predominates as in figure 1.1b, but due to perturbed inflow conditions the outflow variation shows a contradictory trend near the feed (figure 1.1d).

Senecal [7] also investigated the slot type distributor. The basic trends caused by the decrease of the kinetic energy of the fluid along the main channel and by the frictional losses also determine essentially the outflow behavior of the slot dispenser. However, whereas the outflow from the perforated pipe through single holes with relatively small diameter compared to the pipe's wall thickness can always be regarded as perpendicular to the pipe axis, the continuous outflow stream from a slot type dispenser is not forced to be perpendicular to the main channel axis. Depending on the axial extension of the slot the velocity of the exiting fluid stream may have a significant component into axial direction, so that the fluid does not leave the dispenser as a typical planar jet, whose jet exit velocity has no such component into the direction of the planar orifice.

A first detailed analytical description of the flow inside a pipe dispenser was done by Acrivos et al.[1]. They derived a set of balance equations, suitable for describing the behavior of the

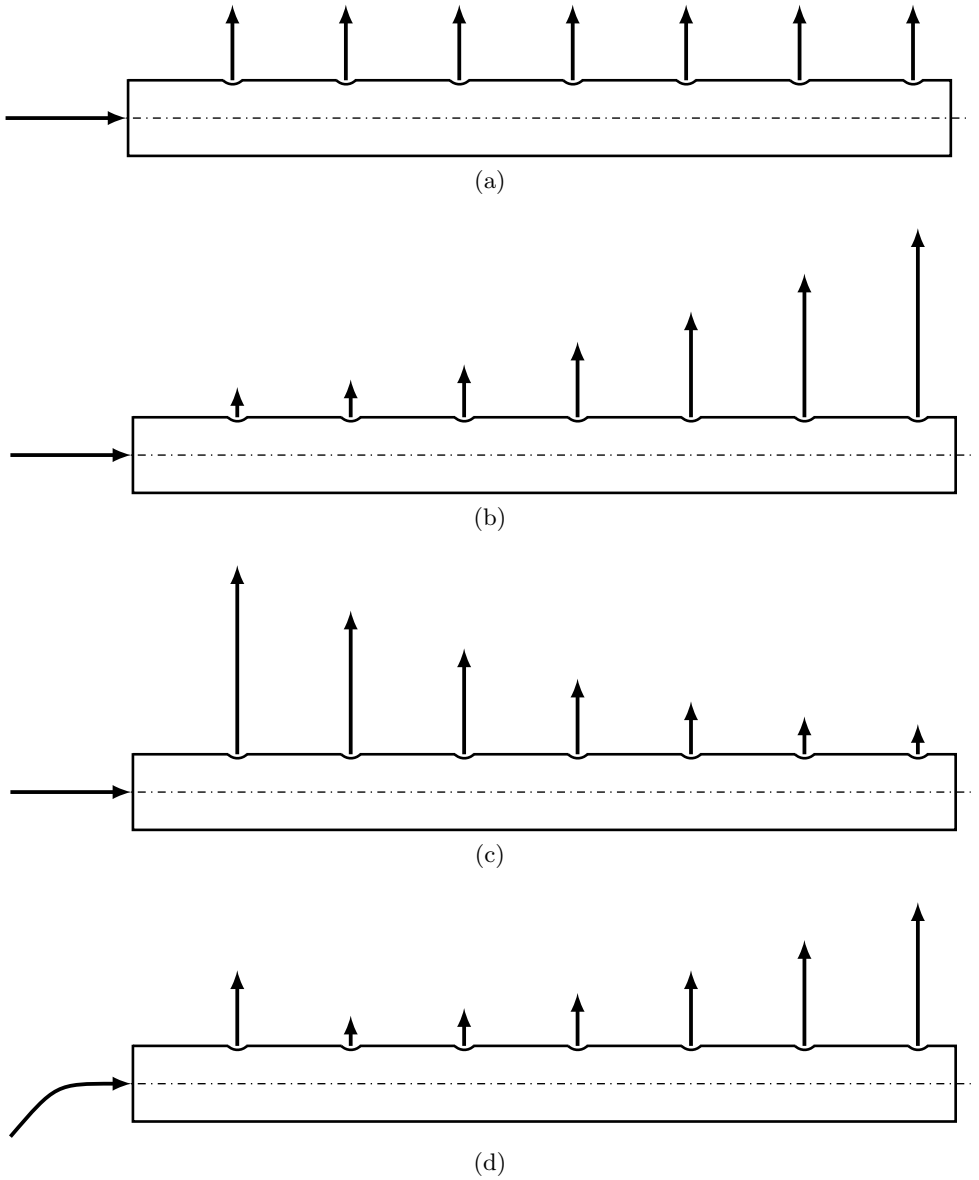

Figure 1.1.: Different types of outflow rate variations of a perforated pipe according to Senecal [7]. (a) uniform distribution, (b) rising outflow rate from the inlet to the end, (c) falling outflow rate from the inlet to the end and, (d) non-monotonous variation of the outflow rates caused by perturbed inflow conditions.

multi-hole and slot dispenser type. Their theory covers the blowing case, where a single inlet stream is divided into multiple outlet streams, as well as the sucking case, where multiple inlet streams are collected to one single outlet stream. The analytical description of the flow inside a pipe dispenser, developed by Acrivos et al. [1], is based on the balances of momentum, kinetic energy and mass, rewritten in the one-dimensional streamtube approximation. For the losses of momentum and kinetic energy, which occur in a real flow due to frictional forces, secondary flows and other flow phenomena not covered by the model, they introduced model parameters in the corresponding equations. The model proposed by Acrivos et al. [1] represents a simplified but still reliable approach, as it essentially describes the main physical mechanisms determine the flow though the manifold. Furthermore, its mathematical formulation is very convenient for being programmed in a code yielding a computationally efficient simulation tool. For both reasons the one-dimensional model of Acrivos et al. [1] was adopted in the present work as well to provide a appropriate description of the fluid flow inside the dispensers investigated in this work. The formulation of this model is described in detail in section 2.1.2. To validate their model Acrivos et al. [1] carried out experiments with a perforated brass pipe. Their experimental data are also used in the present work to verify the computational code which is developed for solving the model formulation proposed by Acrivos et al. [1]. Details of this validation are given in section 3.1. The benefit of simplicity certainly brings about some disadvantage of the model proposed by Acrivos et al. [1]. This model requires a couple of parameters to account for all flow phenomena which cannot be captured by the one-dimensional streamtube approximation. The mainly more-dimensional phenomena may have a significant effect in the investigated dispenser geometries.

A detailed experimental and computational investigation of pipe and ring dispensers was performed by Kulkarni et al. [3]. They compared the pressure profiles along the distributor channels and outflow velocities at the exit ports obtained from their experiments against the results of the model of Acrivos et al. [1], and the results of their CFD calculations, considering ten different straight-pipe dispensers. Kulkarni et al. [3] found that the model proposed by Acrivos et al. [1] is most suitable to predict the behavior of the dispensers. Great deviations between the results obtained with this model and the experimental data were only observed, when the setting of the model parameters significantly differed from the values extracted from the real flow measurements. The actual values of these parameters can vary significantly for different dispenser layouts, as shown by Kulkarni et al. [3]. While Acrivos et al. [1] determined those parameters only based on experiments to calibrate their model, Kulkarni et al. [3] extracted those parameters from CFD calculations as well.

An analytical investigation of the prerequisites for a continuous jet flow exiting from a capillary tube was done by Linblad and Schneider [4]. In their study they examined the uniformity of liquid droplets, which were produced by the capillary breakup of a circular jet under the influence of a periodic disturbance. The investigation of such a capillary brakeup downstream of the nozzle requires a continuous liquid jet flow at the nozzle exit. Linblad and Schneider [4] developed an analytical expression, which allowed them to determine the conditions, where a continuous jet flow at the exit of an arbitrary capillary tube is generated. The expression is derived from an energy balance between the fluid stream inside the tube upstream of the exit denoted by index 1, and a cross-section of the jet of the exit, denoted by index 2, as shown in figure 1.2. The conservation of energy reads:

$$\frac{\mathrm{d}E_{\mathrm{kin},1}}{\mathrm{d}t} = \frac{\mathrm{d}E_{\mathrm{kin},2}}{\mathrm{d}t} + \frac{\mathrm{d}E_{\mathrm{surf},2}}{\mathrm{d}t}, \tag{1.1}$$

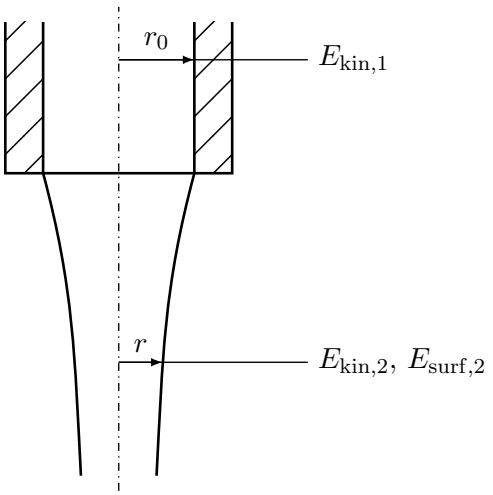

Figure 1.2.: Formation of a single continuous jet at the exit of a capillary tube.

where $\frac{\mathrm{d}E_{\mathrm{kin},1}}{\mathrm{d}t} = \dot{m}\frac{v_1^2}{2}$ represents the flow rate of kinetic energy into the jet from the capillary tube, $\frac{\mathrm{d}E_{\mathrm{kin},2}}{\mathrm{d}t} = \dot{m}\frac{v_2^2}{2}$ the flow rate of kinetic energy at the cross-section 2. $\frac{\mathrm{d}E_{\mathrm{surf},2}}{\mathrm{d}t} = 2r\pi\sigma v_2$ represents the rate of increase of the surface energy associated with the steady formation of new jet surface. Linblad and Schneider [4] stated that for the formation of a continuous jet flow the flow rate of kinetic energy of the fluid stream feeding the jet must be greater than the rate of increase of the jet's surface energy:

$$\frac{\mathrm{d}E_{\mathrm{kin},1}}{\mathrm{d}t} > \frac{\mathrm{d}E_{\mathrm{surf},2}}{\mathrm{d}t}. \tag{1.2}$$

Assuming $v_2 \approx v_1$ for the computation of $\frac{\mathrm{d}E_{\mathrm{surf},2}}{\mathrm{d}t}$ and substituting the mass flow rate $\dot{m} = r^2\pi\rho v_1$ into $\frac{\mathrm{d}E_{\mathrm{kin},1}}{\mathrm{d}t}$ the condition 1.2 can be rewritten as a minimum velocity condition for a continuous jet flow at the exit

$$v_1 > 2\left(\frac{\sigma}{r\rho}\right)^{\frac{1}{2}}, \tag{1.3}$$

dependent of the radius of the jet r, the surface tension σ, and the density of the working fluid ρ. The translation of this criteria into a critical Weber number will be presented in section 2.2.

The stability of an assembly of circular liquid jets against a possible coalescence of individual neighboring jets, as well as a possible transition from a continuous jet flow to a discontinuous dripping mode was examined by Walzel [9]. Based on experiments, where water and water-glycerin mixtures are discharged through an orifice plate into the ambiance, he derived correlations to identify the regime associated with single stable jets without any coalescence of neighboring jets, nor the occurrence of dripping. The relevant dimensionless quantities used to demarcate this regime are the Weber number We, written as

$$We = \frac{\rho v^2 L}{\sigma}, \tag{1.4}$$

the Ohnesorge number Oh

$$Oh = \frac{\mu}{\sqrt{\rho\sigma L}}, \tag{1.5}$$

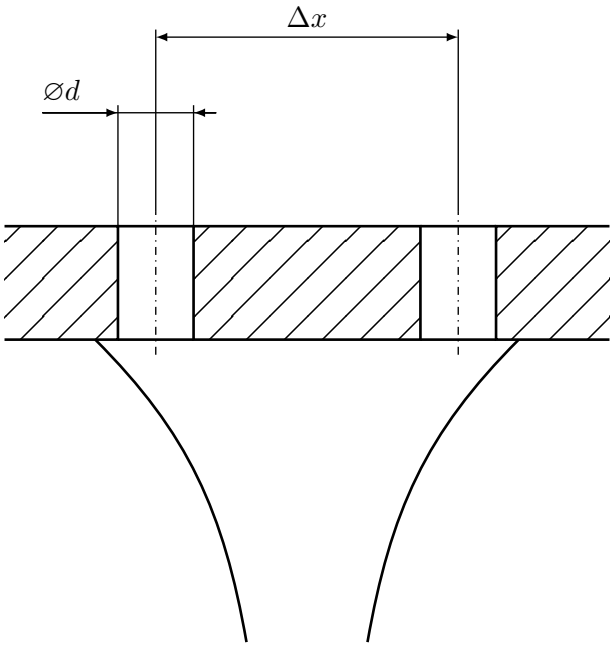

Figure 1.3.: Coalescence of two neighboring circular liquid jets.

and the pitch T

$$T = \frac{\Delta x}{d}. \tag{1.6}$$

The Weber number relates the fluid's inertia to the surface tension (or capillary) forces, with L as characteristic length, e.g., the diameter in case of circular jets, or the width in case of planar jets. The Ohnesorge number (1.5) relates the viscous forces to the surface tension forces. The pitch represents the ratio between the hole distance and the hole diameter. Walzel found the following correlation for the critical Weber number required at minimum for the formation of stable continuous jets at the individual exit holes:

$$We_{\text{crit}} = 14.5 \; Oh^{0.08}. \tag{1.7}$$

For small values of $Oh < 1 \cdot 10^{-3}$ Walzel's correlation (1.7) predicts the formation of a continuous jet in close accordance with relation (1.3) found by Linblad and Schneider [4].

The coalescence of individual neighboring jets is caused by a liquid fillet around each jet, wetting the outer solid surface of the nozzle from which the jet exits. This can be observed at appropriate jet exit velocities as done by Pimbley and Rickenbach [5]. Walzel [9] stated that these fillets can lead to a lamella of liquid between two neighboring jets, if the pitch is below a critical value. This lamella moves in together the jets which it connects. If the kinetic energy of the jets is not sufficient to entrain the lamella in flow direction it adheres at the outer surface of nozzle and leads to a the coalescence of the jets, as shown in figure 1.3. In experiments with different brass showers containing two holes of either diameter 1 or 2 mm, and different values for the pitch Walzel did not observe coalescence between the two jet in any investigated case for a pitch greater than 5. He further stated that a possible coalescence for smaller pitch values can still be avoided by imposing a minimum outflow velocity, which is above the dripping limit. Walzel gave the following equation for determine this minimum

required Weber number, reflecting his experimental results for $T < 5$:

$$We = We_{\text{crit}} + c\,(T-1)^n\,. \tag{1.8}$$

The constants c and n in equation (1.8) are obtained as:

$$\log c = 2 - 2.7\,Oh^{0.48} \tag{1.9}$$

$$n = -\left(1 + 1.6\,Oh^{0.4}\right) \tag{1.10}$$

2. Mathematical formulation

The mathematical formulation presented in this section shall describe the flow of the operating liquid through the dispenser. The flow of the liquid downstream of the exit ports is excluded, so that a single-phase formulation can be used. The governing equations of two alternative approaches, a CFD-based and an appropriate streamtube model based, will be discussed. The last part of this section is denoted to the formulation of the continuous exit jet stability criterion.

2.1. Flow through a multi-hole dispenser

The passage of the fluid through a dispenser with a single inlet hole and multiple outlet holes shall be described here using two different approaches. The first basically most comprehensive description is based on the numerical solution of the three-dimensional Navier-Stokes equations, which can describe the local flow conditions inside the dispenser very accurately. The second computationally less costly approach is based on a one-dimensional description of the flow, where the underlying equations can be solved analytically. The one-dimensional model covers two different types of discharge, the discrete discharge, where the fluid leaves the manifold through multiple individual orifices, and the continuous discharge, where the fluid exits through a single narrow slot. For the discrete discharge the model is also applicable to multi-branch dispensers, where the inlet feed stream is distributed among several manifold branches, and the calculation is done iteratively branch by branch with the overall mass balance as closure condition.

2.1.1. Three-dimensional numerical solution (CFD-based description)

The equations governing the flow of a Newtonian fluid are the continuity equation and the momentum equations termed the Navier-Stokes equations. The present work focuses on steady-state flow of incompressible Newtonian fluids, where the density is constant. In this case the continuity and Navier-Stokes equations may be written as:

$$\vec{\nabla} \cdot \vec{v} = 0, \tag{2.1}$$

$$\left(\vec{v} \cdot \vec{\nabla}\right) \vec{v} = -\frac{1}{\rho}\vec{\nabla} p + \nu \Delta \vec{v}. \tag{2.2}$$

Equations (2.1) and (2.2) form a system of nonlinear partial differential equations for the three unknown components u, v and w of the velocity vector $\vec{v}$ and the unknown static pressure p.

In the CFD-based approach, this system is solved numerically using the finite-volume method. In this method the computational domain is discretized by dividing it into small control volumes defining at the centroid of each volume local nodes, where the unknowns are allocated. Then the governing equations are integrated over each control volume, where fluxes across the faces of each volume are approximated by algebraic expressions, which only contain the

values of the unknowns at the defined nodes. This volumetric integration transforms the governing partial differential equations into a system of algebraic equations, which can be solved numerically.

The coupled system of algebraic equations obtained from the finite-volume based discretization of equations (2.1) and (2.2) is solved using the SIMPLE[1] algorithm. Thereby the momentum and continuity equations are iteratively solved in a segregated manner. Each iterative step consists of solving first the momentum equation for each component of the velocity vector separately, using the known values from previous iterations for the fluxes at cell faces and the pressure. In the second step the predicted velocities are corrected using the continuity equation, so that the obtained new velocities fulfill the mass balance.

The momentum fluxes appearing in the spatial discretization of the momentum equation (2.2) are approximated with second-order accuracy using an Upwind scheme for the convection term $\left(\vec{v}\cdot\vec{\nabla}\right)\vec{v}$ and the pressure term $-\frac{1}{\rho}\vec{\nabla}p$, and a central-difference scheme for the diffusion term $\nu\Delta\vec{v}$. Gradients occurring in these approximations are computed based on a least squares method. The flux terms in the continuity equation are approximated using the Rhie-Chow interpolation method.

The conservation equations represented by (2.1) and (2.2) are suitable for the computation of steady state laminar flow. Extended to a transient formulation they are basically also suitable for describing turbulent flow, but this would require an excessively high number of control volumes to resolve the turbulent motion on all relevant scales. The huge number of control volumes needed for the present problem would lead to unfeasible high computational costs. Therefore, the present work applies the computationally affordable RANS[2] approach, which is widely used for the computation of turbulent flow. The turbulence causes velocity and pressure fluctuations in time. The RANS approach is based on the Reynolds decomposition, where the instantaneous flow quantities are decomposed into a statistical mean value and a turbulent fluctuating contribution written as

$$\vec{v} = \overline{\vec{v}} + \vec{v}', \tag{2.3}$$

$$p = \overline{p} + p'. \tag{2.4}$$

$\overline{\vec{v}}$ and $\overline{p}$ represent time independent statistical averages of the velocity and the pressure, and $\vec{v}'$ and p' represent their fluctuations, respectively. Replacing $\vec{v}$ and p in equations (2.1) and (2.2) by their decompositions (2.3) and (2.4), and averaging the equations over an infinitely long period of time leads to the RANS equations:

$$\vec{\nabla}\cdot\overline{\vec{v}} = 0, \tag{2.5}$$

$$\left(\overline{\vec{v}}\cdot\vec{\nabla}\right)\overline{\vec{v}} + \overline{\left(\vec{v}'\cdot\vec{\nabla}\right)\vec{v}'} = -\frac{1}{\rho}\vec{\nabla}\overline{p} + \nu\Delta\overline{\vec{v}}. \tag{2.6}$$

The nonlinear second term on the left hand side of equation (2.6) represents the momentum transfer associated with the turbulent fluctuating motion. This so called Reynolds stress term involves the nonlinear combination of the velocity fluctuations $\vec{v}'$, which makes the system of equations (2.5)–(2.6) underdetermined. The dynamical effect of the Reynolds stresses is very similar to that caused by the viscous stresses. This led to the Boussinesque "eddy viscosity" concept, which closes the system of equations (2.5)–(2.6) by calculating the Reynolds stresses

[1] SIMPLE abbreviates "Semi-Implicit Method for Pressure-Linked Equations"
[2] RANS abbreviates "Reynolds-Averaged Navier-Stokes"

like the viscous counterparts using an eddy viscosity $\nu_{\text{turbulent}}$. This effectively increases the molecular viscosity ν by the turbulent viscosity $\nu_{\text{turbulent}}$ as follows:

$$\nu_{\text{effective}} = \nu + \nu_{\text{turbulent}}. \tag{2.7}$$

The resulting equations for the mean values have the same form as (2.1) and (2.2), with ν being substituted by $\nu_{\text{effective}}$. A closure model for the turbulent viscosity has still to be provided. The present work applies a well-established standard model, where $\nu_{\text{turbulent}}$ is calculated from the turbulent kinetic energy k and the turbulent dissipation rate ϵ as follows:

$$\nu_{\text{turbulent}} = C_\nu \frac{k^2}{\epsilon}. \tag{2.8}$$

This approach is called the k-ϵ model, with k representing the kinetic energy contained in the turbulent motion, and ϵ representing the specific transfer rate of turbulent kinetic energy from larger to smaller length scales until its final dissipation into viscous heat. C_ν in equation (2.8) is a model constant, which is commonly set to 0.09. In the standard k-ϵ model k and ϵ are computed from corresponding scalar transport equations written as

$$\vec{\nabla} \cdot \left(k\overline{\vec{v}}\right) = \vec{\nabla} \cdot \left[\left(\nu + \frac{\nu_{\text{turbulent}}}{\sigma_k}\right)\vec{\nabla}k\right] + P_k - \epsilon, \tag{2.9}$$

$$\vec{\nabla} \cdot \left(\epsilon\overline{\vec{v}}\right) = \vec{\nabla} \cdot \left[\left(\nu + \frac{\nu_{\text{turbulent}}}{\sigma_\epsilon}\right)\vec{\nabla}\epsilon\right] + C_{\epsilon,1}\frac{\epsilon}{k}P_k - C_{\epsilon,2}\frac{\epsilon^2}{k}. \tag{2.10}$$

σ_k and σ_ϵ are the turbulent Prandtl numbers for the turbulent kinetic energy and turbulent dissipation rate, and are set to 1.0 and 1.3, respectively. P_k represents the rate at which the time averaged strain field produces turbulent kinetic energy. It is calculated as

$$P_k = \nu_{\text{turbulent}} \left\|\boldsymbol{S}\right\|^2, \tag{2.11}$$

where $\boldsymbol{S}$ represents the strain rate tensor

$$\boldsymbol{S} = \frac{1}{2}\left[\vec{\nabla}\ \vec{v} + \left(\vec{\nabla}\ \vec{v}\right)^{\mathrm{T}}\right].$$

$C_{1,\epsilon}$ and $C_{2,\epsilon}$ in equation (2.10) are model constants, which are set to 1.44 and 1.92, respectively.

Due to the fact that the continuity and the momentum equations for turbulent flow modeled with the eddy viscosity concept have the same form as (2.1) and (2.2), their numerical solution is done the same way as described for the laminar case. The solution algorithm has to be only extended for solving the transport equations for k and ϵ. In each iteration, after velocity and pressure are corrected, the transport equations (2.9) and (2.10) are solved. With the new values for k and ϵ the effective viscosity gets updated according to (2.8) before the next iteration starts.

The wall boundaries of the computational domain would basically require no-slip conditions for the velocity of the fluid. Since the k-ϵ model is valid only in the fully turbulent flow region, it cannot be applied down to the viscous sublayer near the wall, where the flow becomes laminar. The wall boundary condition is therefore imposed in a fully turbulent region above the viscous sublayer, where the non-zero velocity can be obtained by the logarithmic law of the wall. Details about the logarithmic law of the wall can be found e. g. in the textbook by Schlichting and Gersten [6].

In the present work all the CFD calculations are carried out with the commercial software Ansys Fluent.

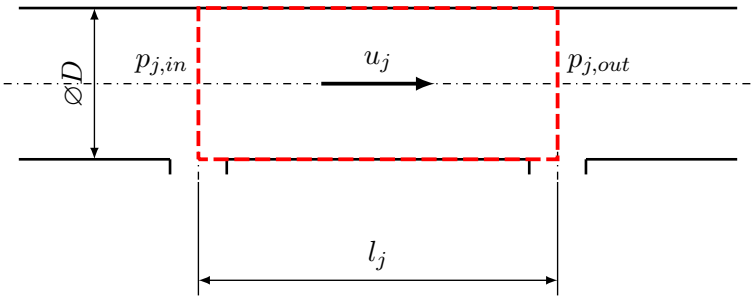

Figure 2.1.: Section j of the distributor channel, located between two outlet ports.

2.1.2. Analytical one-dimensional description

The presently used one-dimensional model describing the flow through manifolds was originally developed by Acrivos et al. [1]. They divide the distributor channel into individual sections $j = 1 \dots J$, each one covering the space between two outlet ports, so that no fluid is branched off within one section, as shown in figure 2.1. The flow inside section j can then be considered as ordinary straight channel flow, which is associated with a loss of static pressure due to friction. According to the extended Bernoulli equation for flow with frictional losses, the loss in static pressure can be written as

$$p_{i,in} - p_{j,out} = \zeta_j \rho \frac{u_j^2}{2}. \tag{2.12}$$

According to equation (2.12) the static pressure loss is equal to the dynamic pressure in section j, $\rho\frac{u_j^2}{2}$, where u_j is the average velocity over the cross section of the channel, multiplied with the pressure loss coefficient ζ_j. For the presently considered case of a straight channel flow, the pressure loss coefficient for section j could be determined as a function of the friction factor λ_j, the section length l_j and the hydraulic diameter $D = \frac{4A}{S}$:

$$\zeta_i = \lambda_j \frac{l_j}{D}. \tag{2.13}$$

For hydraulically smooth channels, which are most common in technical applications and are considered here, the friction factor depends only on the Reynolds number $Re = \frac{uD}{\nu}$. In case of laminar pipe flow, so called Hagen-Poiseuille flow, where $Re < 2300$, the relation between friction factor and Reynolds number can be derived analytically, see e. g., the textbook by Spurk and Aksel [8]. For turbulent flow Blasius developed an empirical correlation, which is valid up to $Re = 10^5$. According to the flow type in section j the friction factor is calculated either with the Hagen-Poiseuille or the Blasius relation:

$$\lambda_j = \begin{cases} \frac{64}{Re_j} & \text{if } Re_j < 2300 \text{ (Hagen-Poiseuille)}, \\ 0.3164 Re_j^{-\frac{1}{4}} & \text{if } 2300 \leq Re_j \leq 10^5 \text{ (Blasius)}. \end{cases} \tag{2.14}$$

Between two adjacent sections, j and $j+1$, a portion of the main stream is leaving the pipe through an outlet port. This leads to a rise in the static pressure in the main channel as the remaining fluid gets decelerated for continuity reasons. This can be described by mass and momentum balances over a control volume containing the outlet port, as shown in figure 2.2.

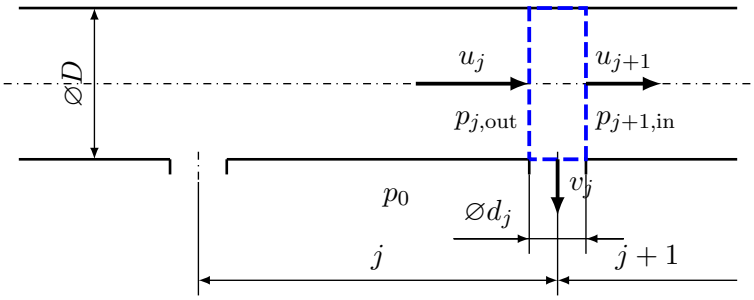

Figure 2.2.: Control volume at an outlet port, located between sections j and $j+1$.

The flow through the control volume containing a discharge exit is governed by the mass balance and the momentum balance in the axial direction written as

$$u_j A = u_{j+1} A + v_j A_j, \tag{2.15}$$

$$p_{j+1,\text{in}} - p_{j,\text{out}} = K_j \left(\rho u_j^2 - \rho u_{j+1}^2\right), \tag{2.16}$$

respectively, where $A = \frac{D^2\pi}{4}$ denotes the channel's cross-sectional area, and $A_j = \frac{d_j^2\pi}{4}$ the cross-sectional area of outlet port j. The momentum balance (2.16) involves the momentum recovery factor K_j, set within $0 \leq K_j \leq 1$, to account for momentum losses appearing in a real flow at the exit hole. Due to these losses the change in axial momentum is not totally transferred into a change of static pressure.

The flow through an outlet port is driven by the pressure difference between the pressure inside the channel and the ambient pressure. Based on the extended Bernoulli-equation for flow with losses, the outflow velocity v_j is related to the pressure difference by

$$v_j = C_j \sqrt{\frac{2}{\rho}\left(\frac{p_{j,\text{out}} + p_{j+1,\text{in}}}{2} - p_0\right)}, \tag{2.17}$$

where the static pressure inside the channel is expressed in terms of the arithmetic mean, $\frac{p_{j,out}+p_{j+1,in}}{2}$. A discharge coefficient C_j, set within $0 \leq C_j \leq 1$, is introduced, which takes into account all losses of the flow passing through the orifice, e. g., caused by secondary flows. These losses effectively reduce the outflow rate for a given pressure difference.

The equations (2.12), (2.15), (2.16) and (2.17), written for each section $j = 1 \ldots J$, constitute a set of equations for the unknowns u_j, v_j, $p_{j,\text{in}}$ and $p_{j,\text{out}}$. This coupled system of equations can be solved iteratively either by varying the inlet pressure in the case of a predefined volumetric inlet flow rate, or by adapting the volumetric flow rate in the case of a fixed inlet pressure. The closure condition for both methods is the overall mass balance:

$$\sum_{j=1}^{J} Q_j = Q. \tag{2.18}$$

Therein, Q is the volumetric flow rate at the entrance of the distributor, and $Q_j = v_j A_j$ is the volumetric flow rate at the exit hole j. If the dispenser consists of multiple distributor branches $i = 1 \ldots I$, an additional iterative loop is necessary to fulfill the mass balance over

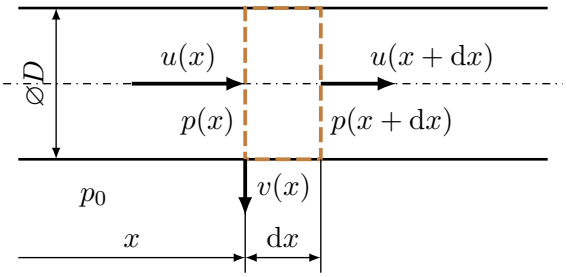

Figure 2.3.: Control volume covering a infinitesimal axial length dx of the continuous manifold.

all branches:

$$\sum_{j=1}^{J} Q_{i,j} = Q_i, \tag{2.19}$$

$$\sum_{i=1}^{I} Q_i = Q. \tag{2.20}$$

The behavior of a spatially continuously dispensing manifold, where the individual outlet ports are replaced by one continuous slot of width b and height h, can also be described by the equations (2.12), (2.15), (2.16) and (2.17), if they are rewritten for a control volume covering an infinitesimal length dx of the manifold as shown in figure 2.3. This leads to the following differential equations for frictional pressure loss

$$p(x) - p(x + \mathrm{d}x) = \lambda(u(x))\frac{\mathrm{d}x}{D}\rho\frac{u^2(x)}{2}, \tag{2.21}$$

mass conservation

$$u(x)A = u(x + \mathrm{d}x)A + v(x)b\mathrm{d}x, \tag{2.22}$$

momentum conservation in the axial direction

$$p(x + \mathrm{d}x) - p(x) = K\left[\rho u^2(x) - \rho u^2(x + \mathrm{d}x)\right], \tag{2.23}$$

and the local outflow velocity

$$v(x) = C\sqrt{\frac{2}{\rho}\left[p(x) - p_0\right]}. \tag{2.24}$$

As indicated in equation (2.14) λ is a function of Re and therefore of $u(x)$. To simplify the formulation of the mass balance the outflow velocity $v(x)$ in (2.22) is assumed invariant inside the control volume. The main difference between the discrete and the continuous formulation is that in the latter the frictional pressure loss does not occur only between two outlet ports. The pressure loss due to friction, described by equation (2.21), and pressure rise due to branching-off of fluid, described by equation (2.23), overlap, so that (2.21) and (2.23) can be combined to

$$p(x + \mathrm{d}x) - p(x) = K\left[\rho u^2(x) - \rho u^2(x + \mathrm{d}x)\right] - \lambda(u(x))\frac{\mathrm{d}x}{D}\rho\frac{u^2(x)}{2}. \tag{2.25}$$

The values at $x + \mathrm{d}x$ can be approximated by Taylor series, truncated after the first order:

$$u(x + \mathrm{d}x) \approx u(x) + \frac{\mathrm{d}u}{\mathrm{d}x}\mathrm{d}x, \tag{2.26}$$

$$p(x + \mathrm{d}x) \approx p(x) + \frac{\mathrm{d}p}{\mathrm{d}x}\mathrm{d}x, \tag{2.27}$$

$$u^2(x + \mathrm{d}x) \approx u^2(x) + 2u(x)\frac{\mathrm{d}u}{\mathrm{d}x}\mathrm{d}x. \tag{2.28}$$

Applying these approximations to equations (2.22) and (2.25) leads to:

$$\frac{\mathrm{d}u}{\mathrm{d}x} = -\frac{b}{A}v(x), \tag{2.29}$$

$$\frac{\mathrm{d}p}{\mathrm{d}x} = -2K\rho u(x) - \frac{\rho}{2D}\lambda(u(x))u^2(x). \tag{2.30}$$

Equations (2.24), (2.29) and (2.30) constitute a system of equations for the three unknowns $u(x)$, $v(x)$ and $p(x)$. Equations (2.29) and (2.30) are first-order differential equations, which need the prescription of boundary values at $x = 0$. For the case of a prescribed volumetric flow rate the boundary value $u|_{x=0}$ is known, and the boundary value $p|_{x=0}$ is calculated iteratively with the overall mass balance used as closure condition.

A solution algorithm for the above described one-dimensional calculations of single-branch multiple hole and slot dispensers, as well as multi-branch multiple hole dispensers has been programmed in Matlab. A detailed description of the algorithm is given in appendix A.

2.2. Stable exit jet flow

To ensure a continuous exit jet flow of a fluid from an orifice Linblad et al. [4] proposed the condition (1.2). This condition is used to compute a critical value for the flow rate of kinetic energy $E_{\mathrm{kin,crit}}$, which has at minimum to be supplied to cover the rate of the increase of surface energy of the liquid jet emanating from the orifice producing continuously new surface.

$$\frac{\mathrm{d}E_{\mathrm{kin,crit}}}{\mathrm{d}t} = \frac{\mathrm{d}E_{\mathrm{surf}}}{\mathrm{d}t} \tag{2.31}$$

For a circular liquid jet which exits from a hole of diameter d at constant mean velocity v, $\frac{\mathrm{d}E_{\mathrm{kin}}}{\mathrm{d}t}$ and $\frac{\mathrm{d}E_{\mathrm{surf}}}{\mathrm{d}t}$ are obtained as

$$\frac{\mathrm{d}E^{\mathrm{cric}}_{\mathrm{kin,\,crit}}}{\mathrm{d}t} = \dot{m}\frac{v^2}{2}, \tag{2.32}$$

$$\frac{\mathrm{d}E^{\mathrm{cric}}_{\mathrm{surf}}}{\mathrm{d}t} = d\pi\sigma v, \tag{2.33}$$

with $\dot{m} = \rho v\frac{d^2\pi}{4}$. Using the definition of the Weber number (1.4) together with (2.32) and (2.33) equation (2.31) gives the following critical limit for the circular jet

$$\left(\frac{\rho v^2 d}{\sigma}\right)_{\mathrm{crit}} = We^{\mathrm{circ}}_{\mathrm{crit}} = 8 \tag{2.34}$$

Walzel [9] found that this theoretical minimum Weber number for the formation of a continuous circular liquid jet reflects the results of his experiments with sufficient accuracy, if the

Ohnesorge number Oh is lower than $1 \cdot 10^{-3}$. For the dispenser design investigated in the present work higher Ohnesorge numbers can be expected. For this the Oh-dependent correlation for the critical Weber number (1.7) presented by Walzel for circular jets will be used in the present work.

For the plane liquid jet the critical Weber number, required at minimum to avoid a transition to dripping, can be obtained in an analogous way to the circular jet. The kinetic energy which is fed into the jet per unit time must be again at minimum equal to the rate of increase of surface energy. For a plane liquid jet exiting from a slot of length l and width b, where $b << l$, at a constant mean velocity v the terms of equation (2.31) are written as

$$\frac{\mathrm{d}E_{\mathrm{kin,\,crit}}^{\mathrm{plane}}}{\mathrm{d}t} = \dot{m}\frac{v^2}{2} = \frac{1}{2}lbhv^3 \tag{2.35}$$

$$\frac{\mathrm{d}E_{\mathrm{surf}}^{\mathrm{plane}}}{\mathrm{d}t} = 2\underbrace{(l+b)}_{\approx l}v\sigma \tag{2.36}$$

Using the definition of the Weber number (1.4) together with (2.35) and (2.36) equation (2.31) yields

$$\left(\frac{\rho v^2 b}{\sigma}\right)_{\mathrm{crit}} = We_{\mathrm{crit}}^{\mathrm{plane}} = 4 \tag{2.37}$$

The multiple single hole dispenser design investigated in this work exhibits a pitch value > 5, so that a possible coalescence of two jets, exiting from neighboring exit holes of the dispenser, can be excluded according to Walzel [9]. The other investigated dispenser type, the narrow slot dispenser, contains only one single plane orifice, so that possible coalescence is not relevant.

3. Test cases and results

At the beginning of this section the developed computational tool for calculating the flow through a multi-hole or slot dispenser, which is based on the one-dimensional theory proposed by Acrivos et al.[1] and described in detail in section 2.1.2, is validated against experimental data. This validation is followed by a presentation and discussion of the computational results obtained from the one-dimensional model and the three-dimensional CFD simulation for two particular nozzle designs, a 7-hole nozzle and a narrow slot nozzle. The presented three-dimensional CFD results are not only used for evaluating the predictions of the one-dimensional model, they also serve to examine the influence of the position of the inlet port on the outflow distribution. In addition to the computational description of the flow through the 7-hole and the slot dispenser, the stability of the individual exiting jets with respect to a possible transition from continuous jet flow to dripping is examined as well, using the criterion described in section 2.2.

3.1. Validation of one-dimensional model against experiments

The experimental data which are presently used for the validation of the one-dimensional model are taken from measurements of Acrivos et al. [1]. They investigated the flow through a perforated pipe. The pipe had a diameter of 26 mm and a length of 1828.8 mm. Twentyfour exit holes of 6.35 mm diameter were drilled into the pipe at a constant axial distance between of 76.2 mm. The working fluid was the ambient air. Acrivos et al. [1] measured the variation of the static pressure along the main channel and the flow rates for various outlet port configurations, ranging from single port discharge to the case with all ports open, for various inlet flow rates. The single port experiments were carried out to determine appropriate values for the discharge coefficient C and the momentum recovery factor K used in their one-dimensional model described in section 2.1.2. The computational code developed in the present work is based on this one-dimensional model. Figure 3.1 shows the experimental data together with the computational results for a volumetric flow rate of $458.3\,\mathrm{l\,min^{-1}}$ imposed at the entrance into the manifold with all twentyfour ports being open. Subfigure 3.1a shows the streamwise variation of the relative static pressure inside the pipe, $\Delta p = p - p_0$, plotted over the axial coordinate x. The subfigure illustrates that Δp is somewhat underestimated by the one-dimensional model. The overall tendency of the static pressure observed in the experiment is still predicted satisfactorily well by the simulation. It has to be noted that agreement could be basically improved by decreasing the discharge coefficient C, whose value was presently adopted directly from the work of Acrivos et al. [1]. The gain in static pressure along the pipe due do the decrease of the mean velocity downstream of each outlet port evidently overcompensates the frictional pressure loss. The variation of the outflow rates is shown in subfigure 3.1b in terms of the relative outflow rate ΔQ_j at each orifice:

$$\Delta Q_j = \frac{Q_j - \bar{Q}}{\bar{Q}}. \tag{3.1}$$

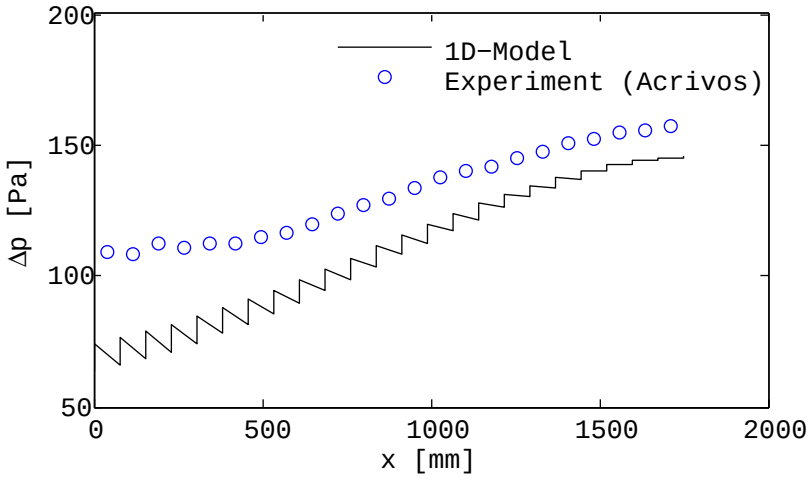

(a)

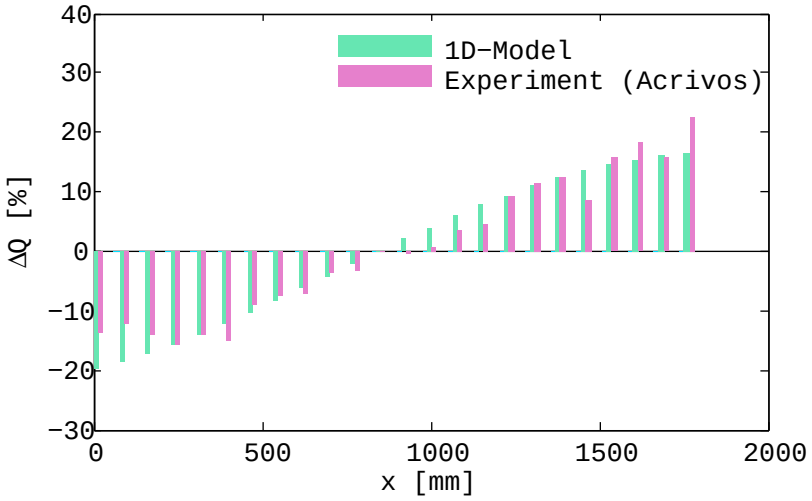

(b)

Figure 3.1.: Computational results of present one-dimensional model compared against experimental data of Acrivos et al. [1]. (a) streamwise variation of the relative static pressure $\Delta p = p - p_0$; (b) relative outflow rates ΔQ_j at the individual exit ports $j = 1 \ldots 24$ (counted from left).

ΔQ_j represents the relative difference between the outflow rate Q_j actually obtained at each exit hole j and a reference value, which represents the uniform distribution and is defined as

$$\bar{Q} = \frac{Q}{J}, \tag{3.2}$$

where J denotes the total number of exit holes. The maximum deviation of the values for ΔQ_j predicted by the simulation from the corresponding experimental data is about 8% indicating a very good agreement. Both the experiment and the computational model exhibit nearly the same streamwise variation of the outflow rate, deviating at maximum about $\pm 20\%$ from the uniform reference flow rate $\bar{Q}$.

3.2. Type A: 7-hole dispenser

The following computational investigations focus a particular dispenser design, which was laid out in cooperation with Lam Research in Villach such that it is readily applicable in the real spinning devices. The dispenser consists of a prismatic main body and an exchangeable orifice plate mounted at the bottom of the body, as shown in figure 3.2. The computational investigation involves two different dispenser configurations. In the first one, denoted with A, the dispenser is equipped with a 7-hole plate. In the second configuration, denoted with B, the 7-hole plate is substituted with a narrow slot plate. These two particular layouts were chosen to serve as a first test bed for the wetting of the wafer with multiple single jets, or a single plane jet. The principle goal of the design was to provide a most uniform distribution of the exit flow rates along the dispenser. Details about the investigation of the dispenser type B are given in section 3.3.

For the type A dispenser, the circular inlet of 5.5 mm diameter is placed alternatively on the top, left, or front face of the dispenser to investigate the influence of the inlet position on the outflow distribution. The distributing main channel is 154 mm long and has a rectangular cross section of 6 mm width and 20 mm height. The dispenser type A is equipped with an orifice plate of 2 mm thickness containing seven holes with a uniform exit diameter $d_j = 1.5$ mm. The distance between adjacent holes is 22.5 mm. The computational flow domain with the alternatively considered inlet ports is depicted in figure 3.3.

The computational investigations are based on the two different approaches, the three-dimensional CFD-based approach, and the one-dimensional model based approach, as described in sections 2.1.1 and 2.1.2, respectively. The one-dimensional model requires the discharge coefficient and the momentum recovery factor as input parameters. The discharge coefficients for the two considered orifice layouts are determined from separately performed two-dimensional CFD simulations. The momentum recovery factor is set to $K = 1.0$, which represents the theoretical upper limit, where the increase in the static pressure due to the branching-off of fluid through the exit holes, as described in section 2.1.2, is highest. The outflow distributions determined with the one-dimensional method for the 7-hole nozzle plate are compared against the corresponding results obtained from the three-dimensional CFD calculation. The working fluid is always liquid water at 20 °C, as the working fluids used in the various spin processing steps applied to the wafers in the real device are mainly aqueous solutions. The total volumetric flow rate Q introduced at the inlet of the dispenser is also chosen to match typical values met in the real process. Accordingly, Q is varied from 500 to 2000 ml min^{-1} with a step size of 500 ml min^{-1}. The boundary condition at the outlets is the

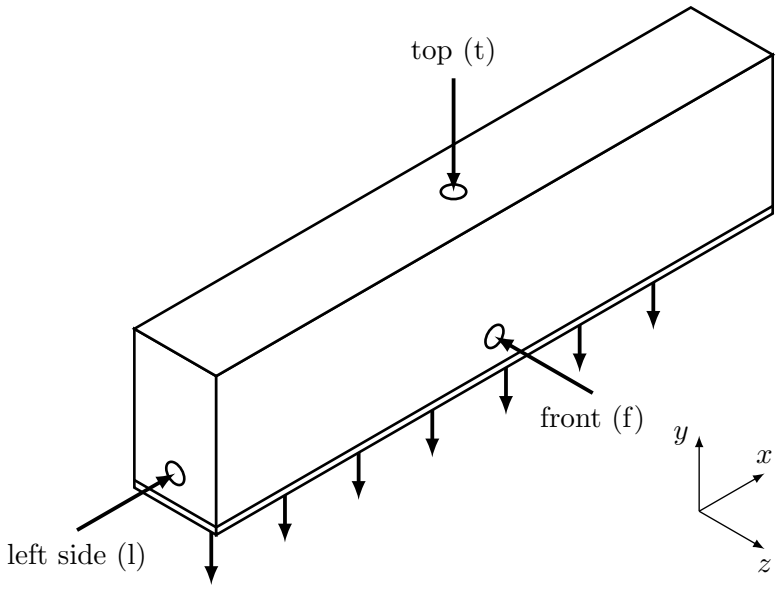

Figure 3.2.: Dispenser body with three alternative inlet positions.

Q	Type A: 7-hole plate		
$\mathrm{ml\,min^{-1}}$	inlet top	inlet left	inlet front
500	A1t	A1l	A1f
1000	A2t	A2l	A2f
1500	A3t	A3l	A3f
2000	A4t	A4l	A4f

Table 3.1.: Dispenser type A: considered test cases

static pressure at ambient atmospheric conditions. All considered cases for the dispenser type A are summarized in table 3.1.

The solution of the flow through the dispenser using the one-dimensional approach requires the discharge coefficient C as input parameter. In the present work this parameter is determined from a separate CFD simulation of the outflow from a reservoir through a single orifice. The reservoir is represented by a cylinder of $D_{\mathrm{reservoir}} = 20\,\mathrm{mm}$ diameter and 10 mm height, as shown in figure 3.4. The orifice has a cone-shaped entrance section with a 90° cone angle. For this particular configuration the flow field can be assumed axisymmetric, which allows for a two-dimensional simulation. The top face of the reservoir, which is marked yellow in figure 3.4, represents the inlet boundary. The outlet is the exit cross-section of the orifice, which is marked green in figure 3.4. At the inlet the velocity normal to the boundary is set to a constant value v_{in}. For each total volumetric flow rate prescribed in the cases A1–A4, a corresponding value for v_{in} is computed as

$$v_{\mathrm{in}} = \frac{Q}{J A_{\mathrm{reservoir}}},$$

assuming a uniform volumetric exit flow rate at all $J = 7$ orifices. $A_{\mathrm{reservoir}} = \frac{D^2_{\mathrm{reservoir}}\pi}{4}$ is the cross-sectional area of the reservoir. At the outlet the gauge pressure is set to 0 Pa. For all cases the flow at the inlet is assumed laminar. In the cases A3 and A4 the flow inside the orifice

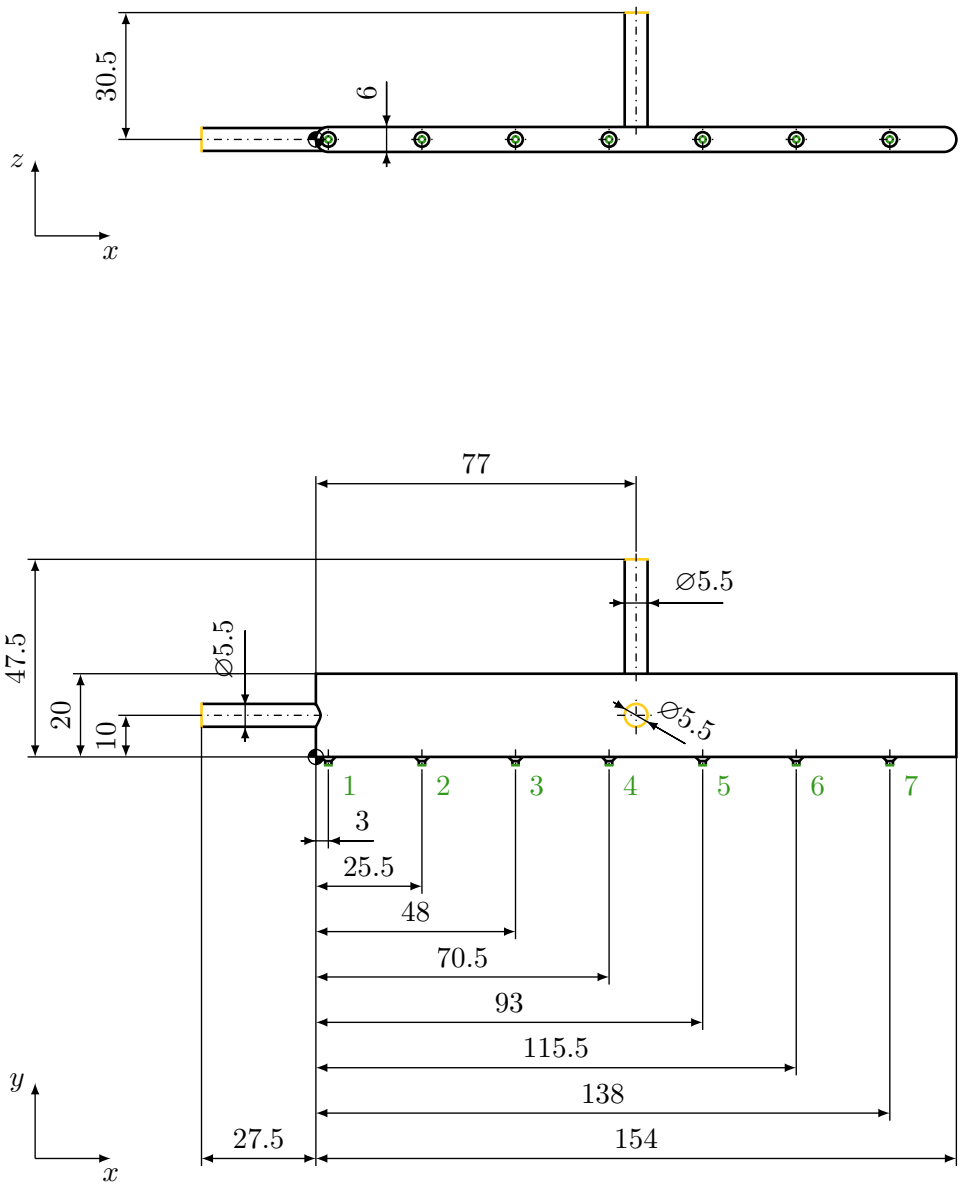

Figure 3.3.: Computational flow domain for the dispenser type A with the alternatively considered three inlet ports (– inlet, – outlet).

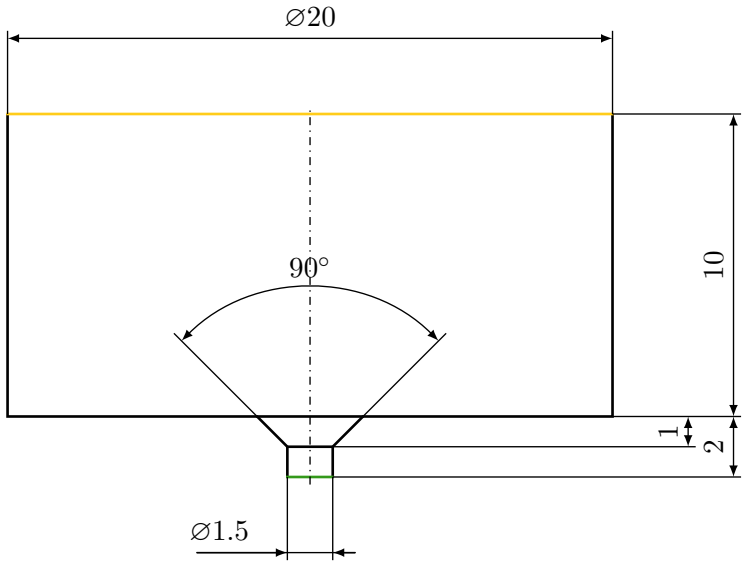

Figure 3.4.: Computational flow domain of the 2D-CFD calculation of the flow from a reservoir through a single outlet orifice (– inlet, – outlet).

Case	C
A1	0.82
A2	0.86
A3	0.87
A4	0.89

Table 3.2.: Dispenser type A: discharge coefficient C for a single orifice obtained from the 2D-CFD simulation.

becomes turbulent, which is taken into account by using the turbulent model described in section 2.1.1. With the data obtained from this 2D-CFD simulation, the discharge coefficient for the single orifice was calculated according to equation (2.17). The resulting discharge coefficients for the cases A1–A4 are listed in table 3.2. The shown values are used for the setting of the discharge coefficients C in the computations of the corresponding cases with the one-dimensional model.

3.2.1. Cases A1t–A4t: Inlet on the top face

For the one-dimensional calculation the dispenser is divided into two branches, with the first one including the orifices number 1–4 to the left of the inlet, and the second one covering the orifices number 5, 6 and 7 to the right of the inlet, as shown in figure 3.3.

The results for the cases A1t–A4t are illustrated in figures 3.5–3.8, with the red lines and red bars referring to the one-dimensional calculation, and the blue lines and blue bars referring to the CFD simulation. The upper subfigures 3.5a–3.8a show the relative static pressure in the main channel averaged over the cross section, $\Delta p = p - p_0$, as a function of the axial coordinate x. The static pressure level obtained from the CFD simulation is always higher as the one obtained from the one-dimensional model. This particular feature will be observed in

all further considered cases for the 7-hole dispenser as well. It makes evident that the discharge coefficients computed from a separate axisymmetric simulation (see table 3.2) for use in the one-dimensional model are generally higher than the values which could be extracted from the cross-sectional averages of the pressure and the exit flow rates of the CFD. It is conceivable that the more complex three-dimensional flow conditions immediately upstream of the exit holes, which can be only captured by a three-dimensional CFD, may effectively reduce the outflow through the orifices leading to smaller discharge coefficients. For all cases A1t–A4t the one-dimensional calculation predicts that the static pressure level is stepwise increased from the inlet towards both ends at each exit hole. This indicates that the increase in pressure at each individual outlet always overcompensates the frictional pressure loss in the channel sections between the outlets. A local increase in the pressure at the outlets can also be seen in the CFD results, but the increase is generally less pronounced than in the one-dimensional analytical solution, which can be attributed to the more complex three-dimensional flow pattern in the main channel. The most obvious discrepancy between the one-dimensional model and the CFD simulation is the peak in the pressure profile near $x = 77$, where the inlet is located. This significant peak is caused by the incoming flow which enters the domain like a vertical submerged jet. The strong vertical inflow hits the bottom of the main channel, so that a stagnation point with a high local static pressure occurs. For the case A3t this vertical jet like inflow is exemplarily illustrated by velocity contours in figure 3.9.

Subfigures 3.5b–3.8b show the calculated outflow distribution in terms of the relative outflow rate ΔQ_j at each orifice as defined in equation 3.1. The red bars in figures 3.5b–3.8b represent the results obtained from the one-dimensional calculation, and the blue ones those obtained from the CFD simulation. The outflow variations obtained from the one-dimensional model for the cases A1t–A4t essentially reflect the tendencies of the static pressure. So the stepwise increase of the pressure level between the exit ports always leads to an increase of the relative outflow rates through the exit holes downstream. This behavior has to be expected in the one-dimensional approach, as can be directly seen from the mathematical formulation in section 2.1.2, where the outflow at each exit hole is computed only as a function of the relative static pressure. The CFD calculation basically exhibits the same behavior, as streamwise increase of the static pressure is again followed by streamwise increase of the relative outflow rates through the exits. For all cases A1t–A4t the CFD results exhibit a peak in the relative high static pressure at the stagnation point opposed to the inlet port, located at $x = 77$. This always leads to a significantly higher outflow rate at the orifice 4, which is closest to this point. The observed strongly increased outflow rate through the exit beneath the inlet port is also the reason for a higher degree of non-uniformity in the outflow distribution exhibited by the CFD results. Quantitatively, the relative deviation from a uniform outflow rate is still fairly small in both computational results. For all cases A1t–A4t the maximum relative difference of the outflow rates is approximately 1% and 5% for the one-dimensional model and the CFD results, respectively.

The minimum Weber number required for the formation of a stable continuous jet flow at the exit holes was calculated according to equation (1.7) using the material properties of the working fluid and the orifice diameter as input parameters. This gave a critical Weber number $We_{\text{crit}} = 9.1$. The Weber numbers obtained from the CFD results for each exiting jet from the 7-hole dispenser for the cases A1t–A4t are listed in table 3.3. For the case A1t the obtained exit Weber numbers come very close to the critical value. This small Weber number regime also implies that a capillary breakup of the jets soon after leaving the outlets has to be expected for this case.

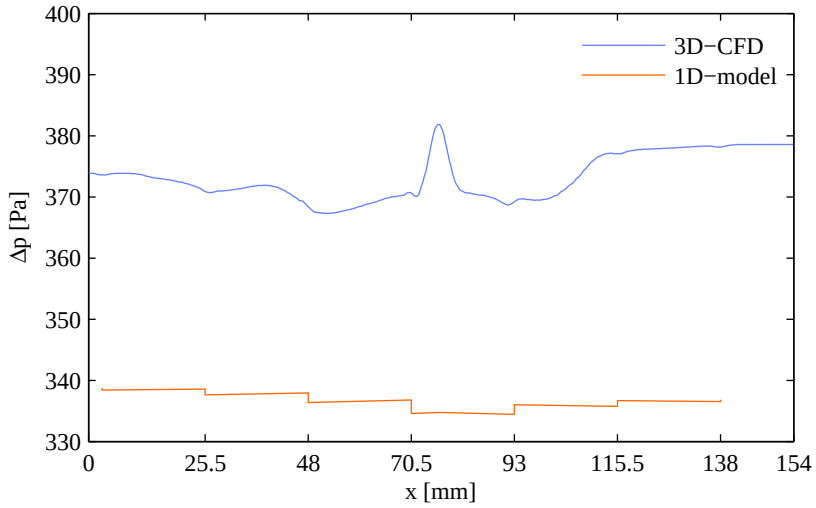

(a)

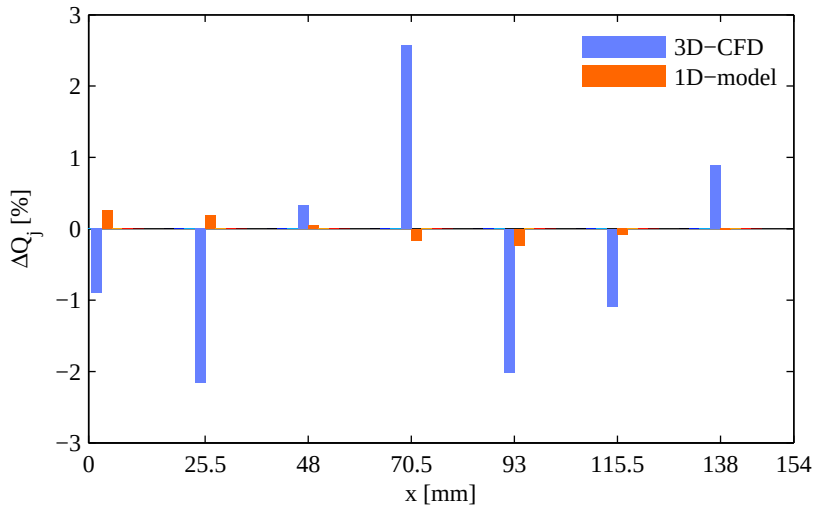

(b)

Figure 3.5.: Case A1t: (a) streamwise variation of the relative static pressure $\Delta p = p - p_0$; (b) relative outflow rate ΔQ_j at the individual exits $j = 1 \ldots 7$ (counted from left).

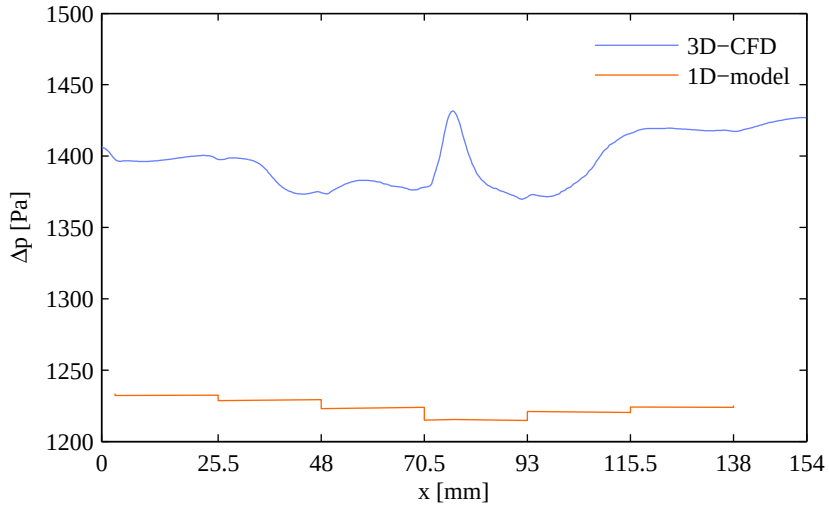

(a)

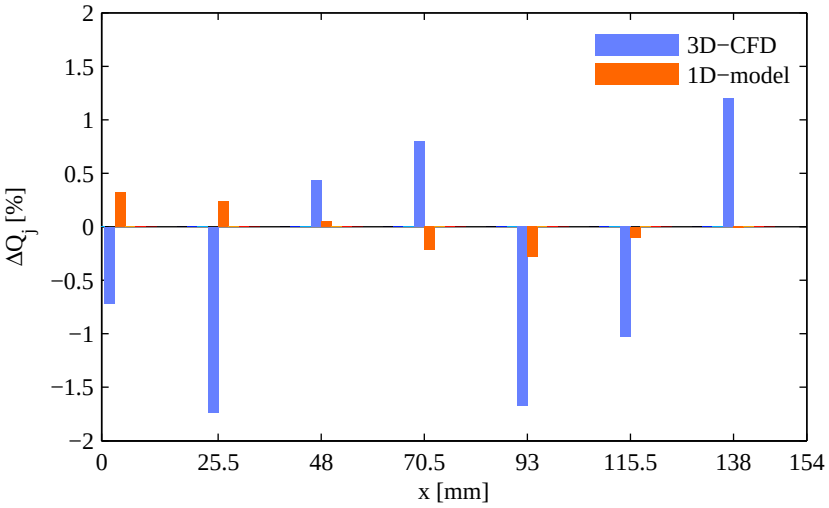

(b)

Figure 3.6.: Case A2t: (a) streamwise variation of the relative static pressure $\Delta p = p - p_0$; (b) relative outflow rate ΔQ_j at the individual exits $j = 1 \ldots 7$ (counted from left).

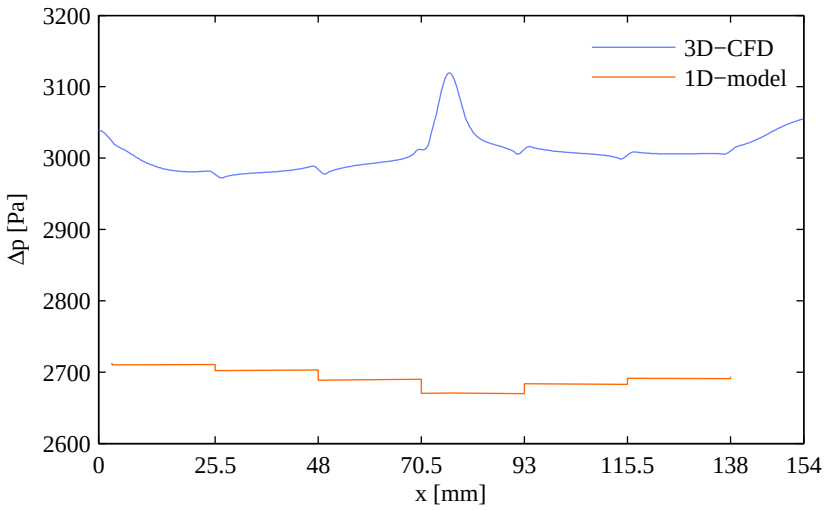

(a)

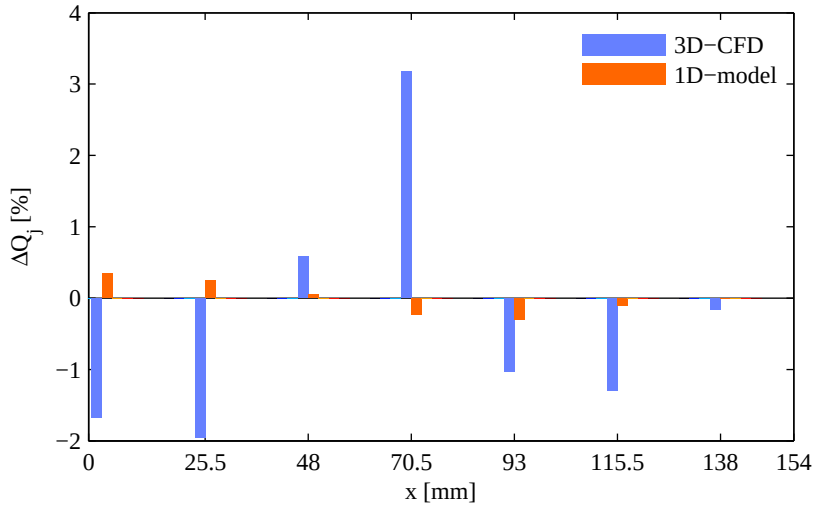

(b)

Figure 3.7.: Case A3t: (a) streamwise variation of the relative static pressure $\Delta p = p - p_0$; (b) relative outflow rate ΔQ_j at the individual exits $j = 1 \ldots 7$ (counted from left).

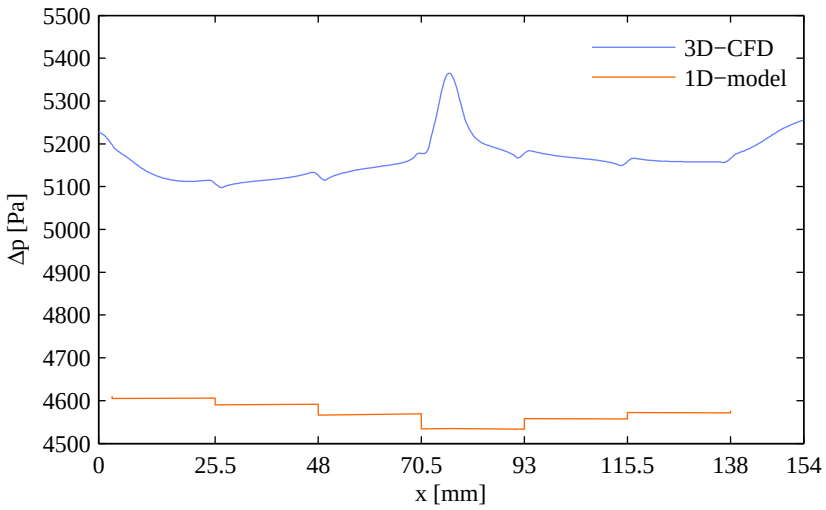

(a)

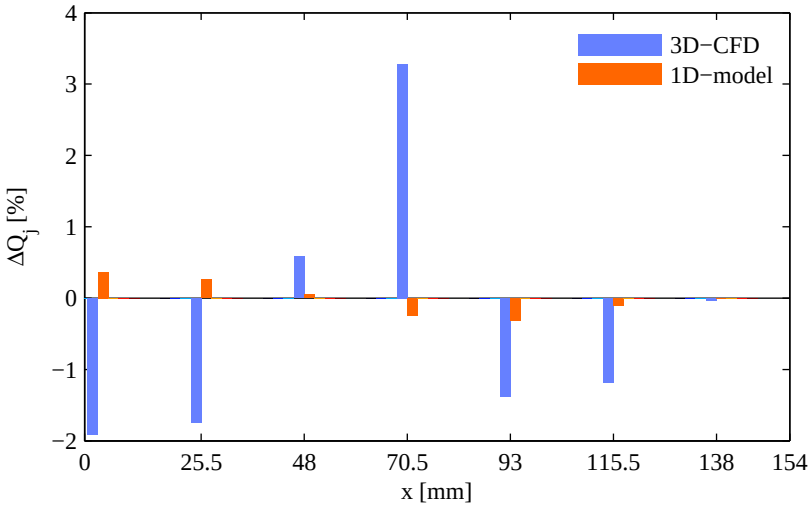

(b)

Figure 3.8.: Case A4t: (a) streamwise variation of the relative static pressure $\Delta p = p - p_0$; (b) relative outflow rate ΔQ_j at the individual exits $j = 1 \ldots 7$ (counted from left).

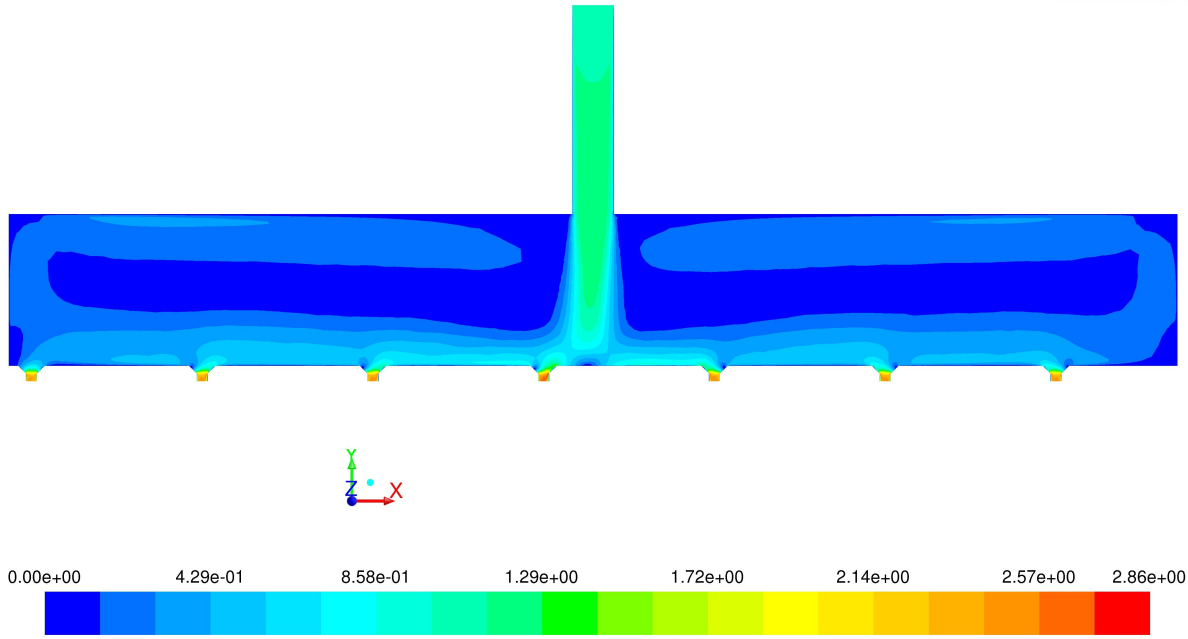

Figure 3.9.: Case A3t: contours of velocity magnitude in $\mathrm{m\,s^{-1}}$ at the midplane of the channel at $z = 0$ obtained from CFD.

Case	*We*						
	1	2	3	4	5	6	7
A1t	9.3	9.0	9.5	9.9	9.1	9.2	9.6
A2t	37.2	36.4	38.1	38.4	36.5	37.0	38.7
A3t	82.1	81.6	85.9	90.4	83.2	82.7	84.7
A4t	145.2	145.8	152.7	161.0	146.8	147.4	150.9

Table 3.3.: Cases A1t–A4t: jet exit Weber numbers *We* at the orifices 1–7 obtained from the CFD results.

3.2.2. Cases A1l–A4l: Inlet on the left side

Assuming the inlet on the left side as shown by figure 3.3 the dispenser can be calculated in the one-dimensional approach using a single branch, which contains all seven orifices. The results for the cases A1l–A4l are illustrated in figures 3.10–3.13 the same way as in the previous section for the cases with the top inlet. The relative static pressures obtained from the CFD simulation are again always higher than those obtained from the one-dimensional model. For the cases A1l–A4l the one-dimensional calculation predicts again a stepwise increase of the static pressure level in the streamwise direction caused by the branching-off of fluid at the individual exits. A streamwise increase of the pressure can also be seen in the CFD results, although the stepwise changes at the individual exit ports are considerably blurred by the complex three dimensional flow effects especially near the inlet. As seen from the velocity contours in figure 3.14, the fluid enters the domain again in a jet-like manner, which leads to a region of separated flow with a local minimum in the pressure at the corner near the inlet. Due to the vertical outflow through the exit holes the initially horizontal jet stream

is directed towards the bottom leading to an increase in the pressure to a local maximum. Subfigures 3.10b–3.13b show the calculated outflow distribution. The variations of the relative outflow rate obtained from the one-dimensional model for the cases A1l–A4l clearly follow the streamwise increase of the corresponding static pressure level. This behavior was already seen and explained by the formulation of the one-dimensional approach for the cases with the inlet on the top in section 3.2.1. The results of the 3D-CFD do not show such a monotonous streamwise increase in the relative outflow rates. This is due to the aforementioned horizontal jet-like inlet stream, which is deflected downwards by the vertical exit streams. The local maximum in the static pressure occurring in the region, where the deflected inlet jet stream hits the bottom, always leads to a significantly increased outflow rate at the exit hole nearest by. The occurrence of such a local maximum flow rate at the exits 2 or 3 prohibits a steady increase of the outflow rates in the streamwise direction featured by the one-dimensional computation, which by definition cannot account for the more-dimensional flow phenomena near the inlet like the 3D-CFD. The maximum quantitative variation of the relative outflow rates is for all cases A1l–A4l approximately 2% and 6% for the one-dimensional model and the CFD results, respectively.

The minimum Weber number required for the formation of a stable continuous jet flow at the exit holes is calculated from equation (1.7) and remains the same as for the cases with the inlet on the top, $We_{\mathrm{crit}} = 9.1$, as the nozzle diameter is the same. The Weber numbers obtained from the CFD results for each exiting jet from the 7-hole dispenser for the cases A1l–A4l are listed in table 3.4. For the case with the lowest inlet flow rate A1l the obtained Weber numbers come closest to the critical value We_{crit}, so that a capillary breakup of the jets right after leaving the outlets has to be expected here.

Case	*We*						
	1	2	3	4	5	6	7
A1l	8.9	9.6	10.0	9.4	9.2	9.3	9.8
A2l	35.2	39.3	37.5	37.2	36.5	37.4	39.4
A3l	81.0	84.5	87.2	83.3	84.3	86.5	90.0
A4l	142.2	148.8	154.0	146.6	148.1	152.0	158.2

Table 3.4.: Cases A1l–A4l: jet exit Weber numbers *We* at the orifices 1–7 obtained from the CFD results.

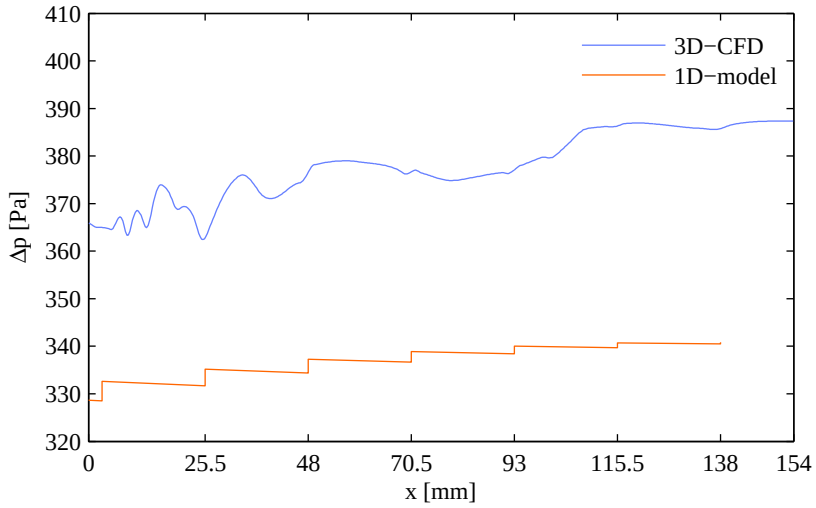

(a)

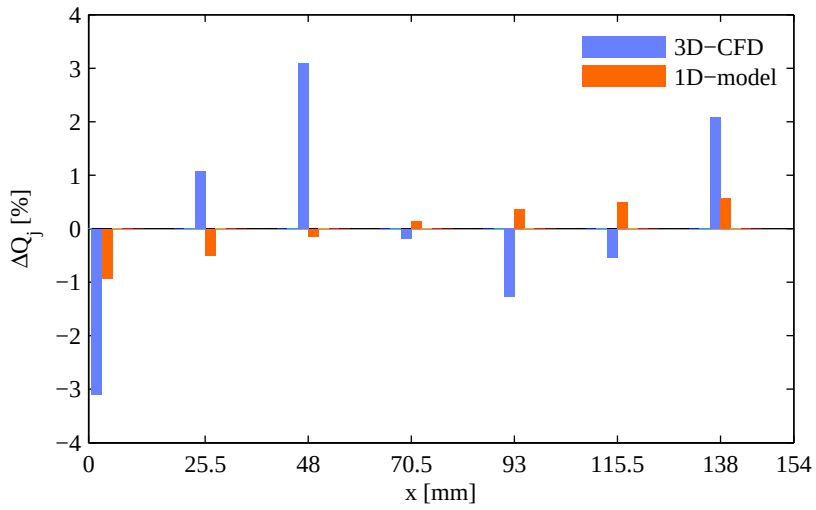

(b)

Figure 3.10.: Case A1l: (a) streamwise variation of the relative static pressure $\Delta p = p - p_0$; (b) relative outflow rate ΔQ_j at the individual exits $j = 1 \ldots 7$ (counted from left).

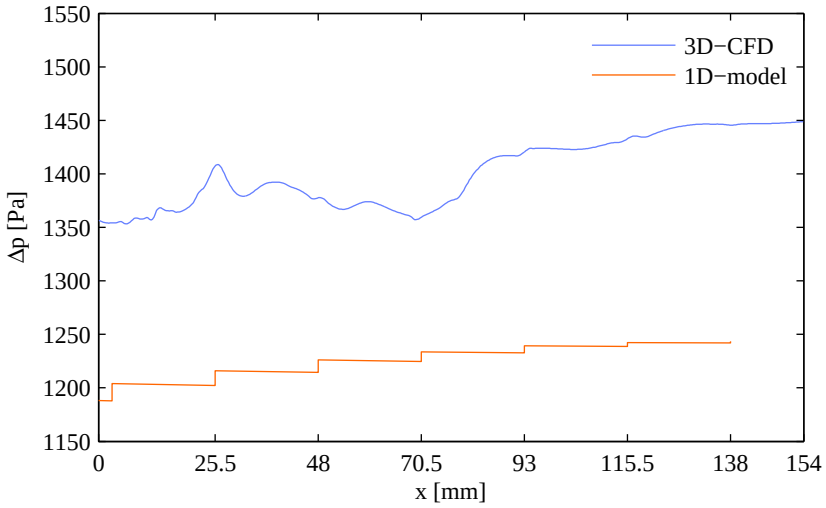

(a)

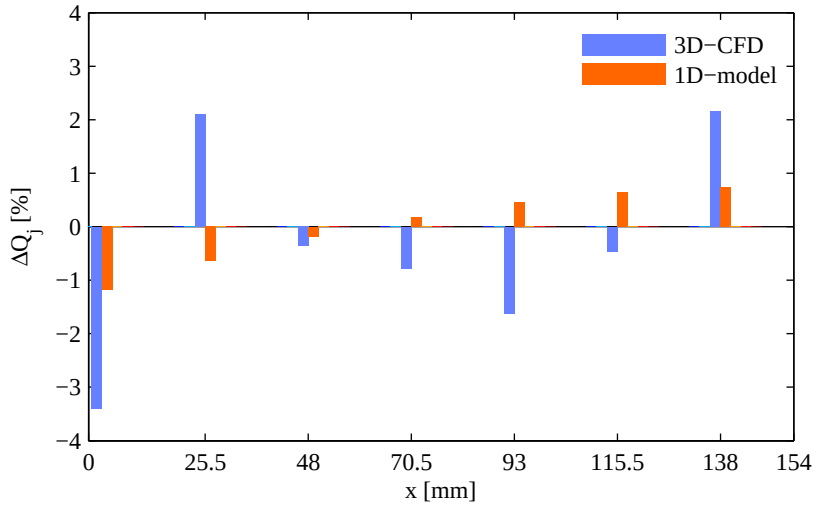

(b)

Figure 3.11.: Case A2l: (a) streamwise variation of the relative static pressure $\Delta p = p - p_0$; (b) relative outflow rate ΔQ_j at the individual exits $j = 1 \ldots 7$ (counted from left).

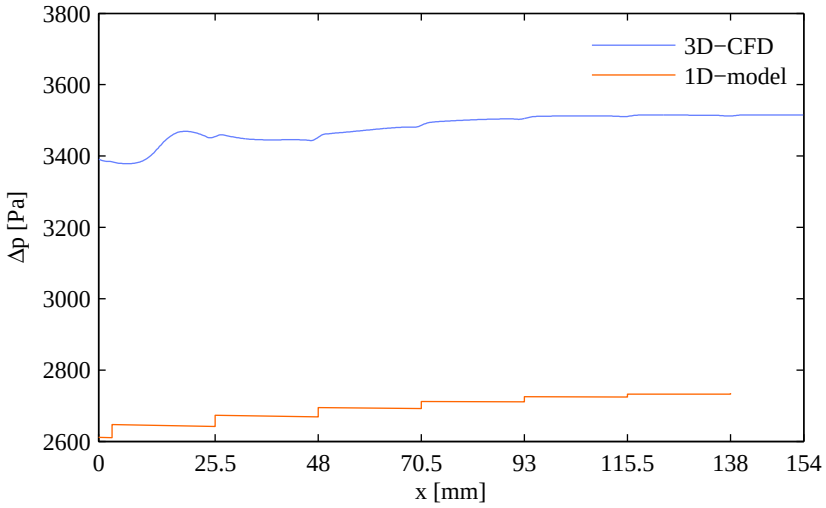

(a)

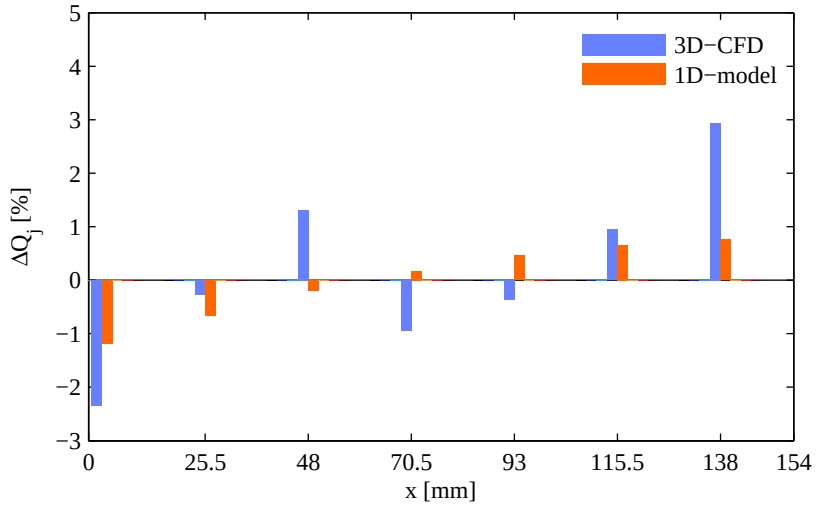

(b)

Figure 3.12.: Case A3l: (a) streamwise variation of the relative static pressure $\Delta p = p - p_0$; (b) relative outflow rate ΔQ_j at the individual exits $j = 1 \ldots 7$ (counted from left).

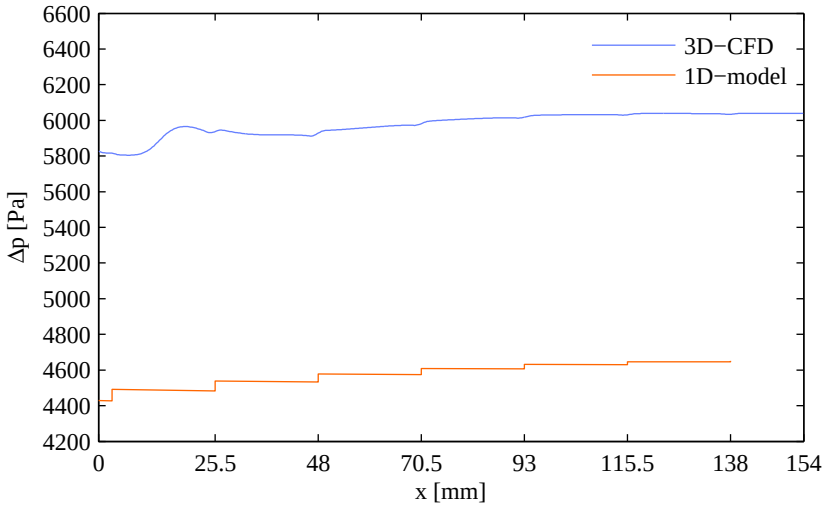

(a)

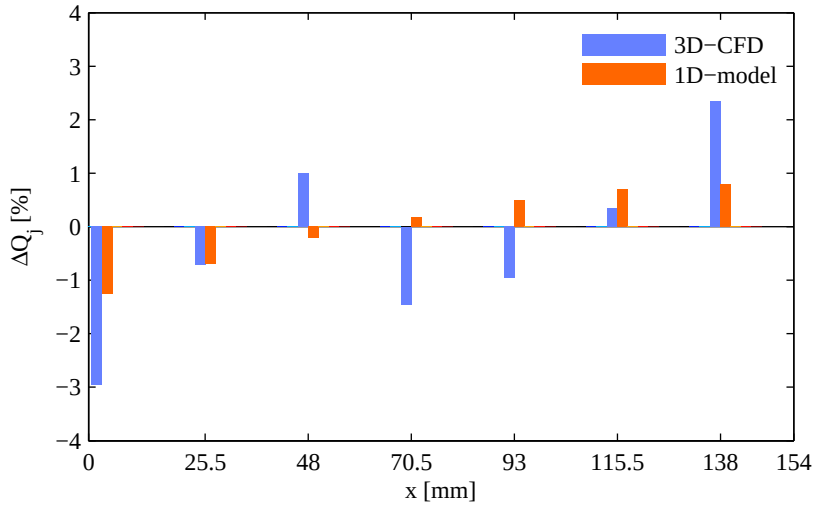

(b)

Figure 3.13.: Case A4l: (a) streamwise variation of the relative static pressure $\Delta p = p - p_0$; (b) relative outflow rate ΔQ_j at the individual exits $j = 1 \ldots 7$ (counted from left).

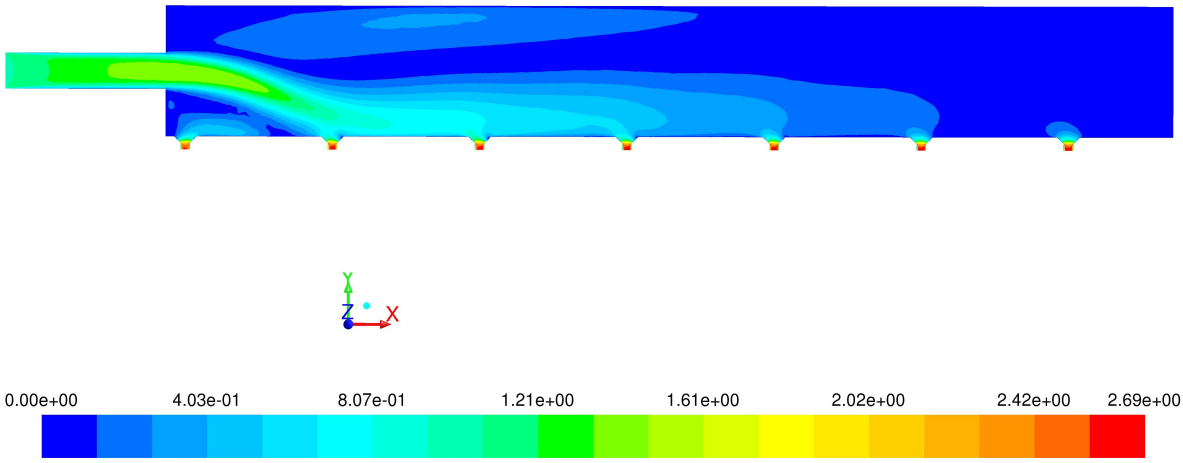

Figure 3.14.: Case A3l: contours of velocity magnitude in $\mathrm{m\,s^{-1}}$ at the midplane of the channel at $z = 0$ obtained from the CFD.

3.2.3. Cases A1f–A4f: Inlet on the front face

The inlet on the front face has exactly the same axial position as for the cases with the inlet on the top of the channel. In the one-dimensional computation the dispense of the incoming liquid is again divided into two branches. The results for the cases A1f–A4f are illustrated in figures 3.15–3.18. The results of the one-dimensional calculation are exactly the same as for the cases with the inlet on the top, because the the one-dimensional approach only accounts for the the position of the inlet in the streamwise direction, which is for both inlet types the same. In contrast, the effect of the horizontal inflow into the dispenser becomes very evident in the three-dimensional CFD results. The horizontally injected fluid hits the back wall of the channel leading to a significant peak in the pressure in the impingement region. Otherwise, the static pressure exhibits a increasing trend towards both ends of the channel similar to the one-dimensional results. The jet-like inlet stream and the impingement on the opposed back wall are illustrated by the velocity contours in figure 3.19 for the case A3f. Subfigures 3.15b–3.18b show the calculated outflow distribution for inlet on the front face. While the one-dimensional results are exactly the same as for the cases with the inlet on the top, the CFD results differ significantly. At $x = 77$, where the static pressure has a maximum, the outflow rate at the nearest exit shows a minimum, which is completely different to the cases A1t–A4t, where the peak pressure always led to a maximum outflow in this section. The horizontally orientated motion of the inlet stream does evidently not translate into a strong motion downwards towards the exit holes beneath the inlet. For all cases A1f–A4f the outflow rates obtained from the one-dimensional model and from the CFD very within a range of approximately 1% and 3%, respectively.

The jet exit Weber numbers obtained from the CFD results at the individual orifices are summarized in table 3.5. As already observed for the previous inlet types, the case with lowest flow rate A1f yields exit Weber numbers closest to the critical value $We_{\mathrm{crit}} = 9.1$.

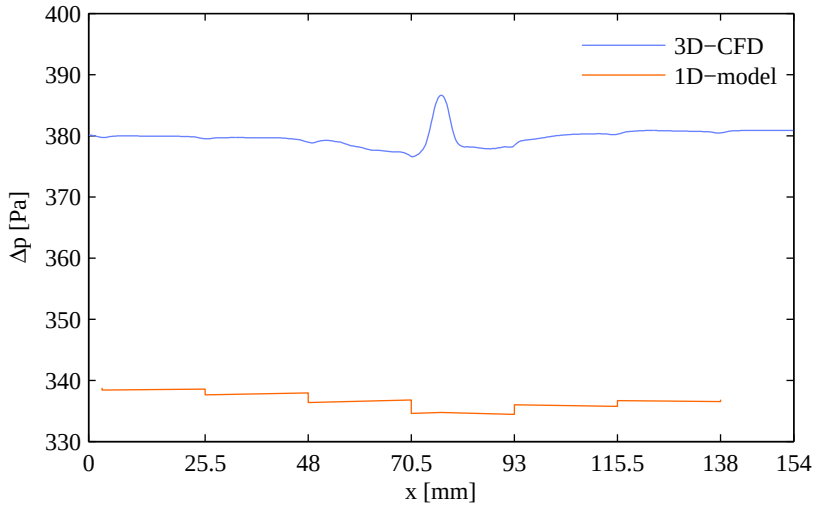

(a)

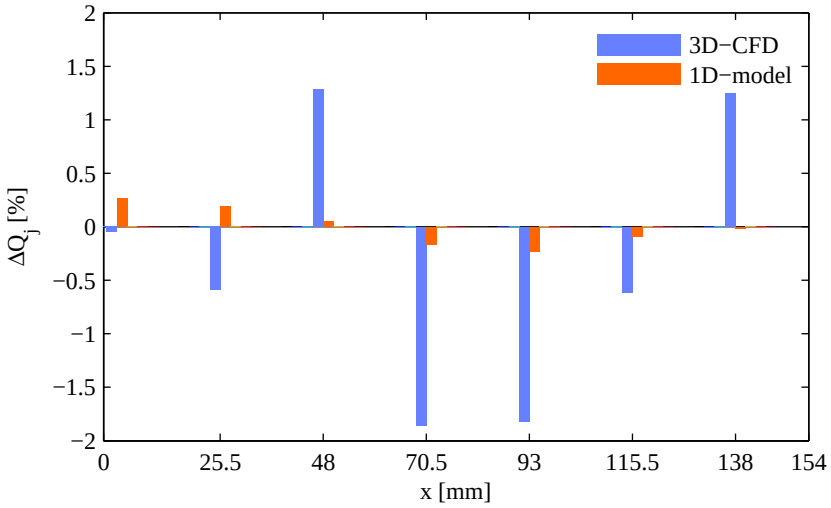

(b)

Figure 3.15.: Case A1f: (a) streamwise variation of the relative static pressure $\Delta p = p - p_0$; (b) relative outflow rate ΔQ_j at the individual exits $j = 1 \ldots 7$ (counted from left).

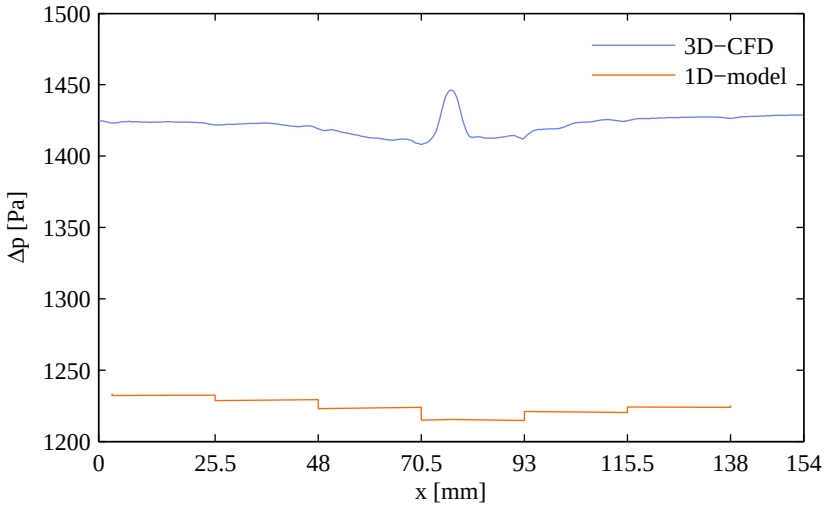

(a)

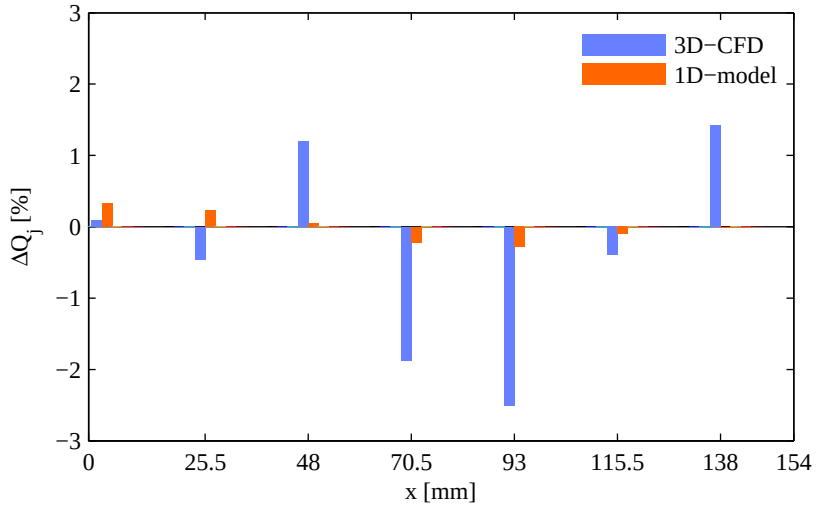

(b)

Figure 3.16.: Case A2f: (a) streamwise variation of the relative static pressure $\Delta p = p - p_0$; (b) relative outflow rate ΔQ_j at the individual exits $j = 1 \ldots 7$ (counted from left).

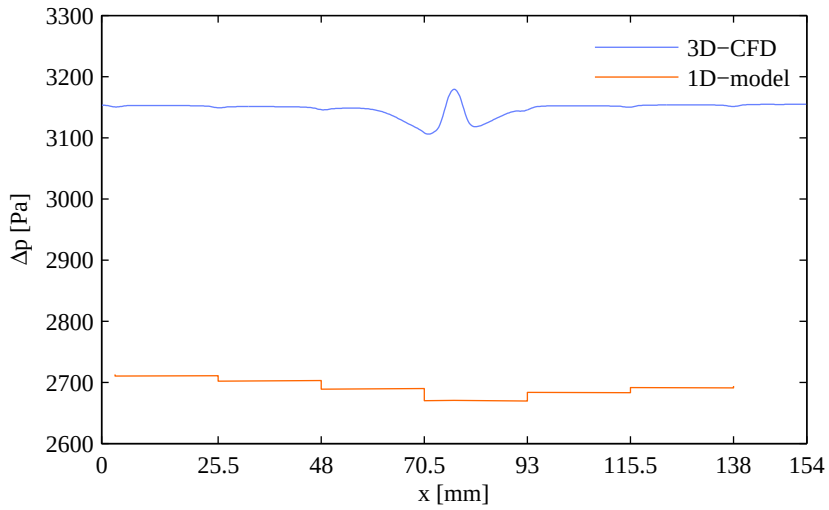

(a)

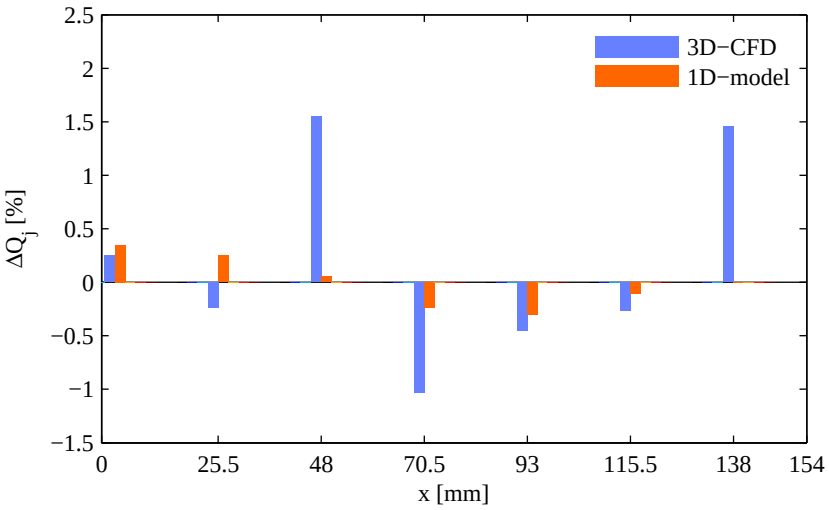

(b)

Figure 3.17.: Case A3f: (a) streamwise variation of the relative static pressure $\Delta p = p - p_0$; (b) relative outflow rate ΔQ_j at the individual exits $j = 1 \ldots 7$ (counted from left).

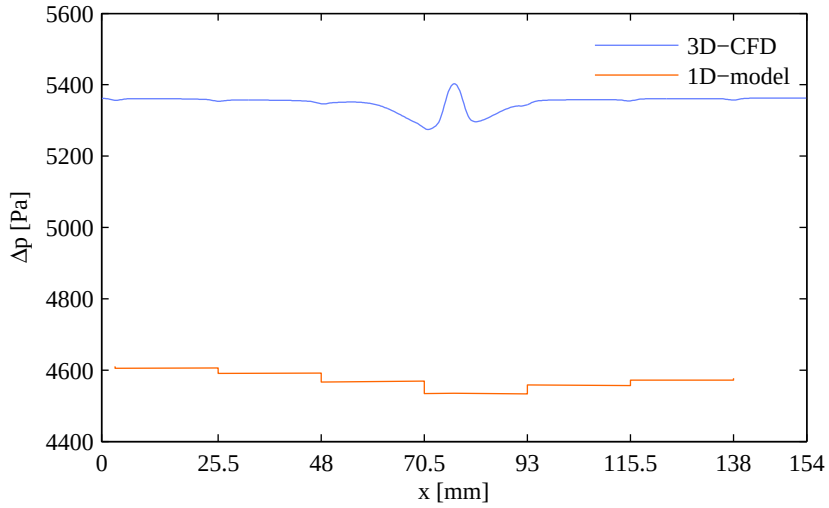

(a)

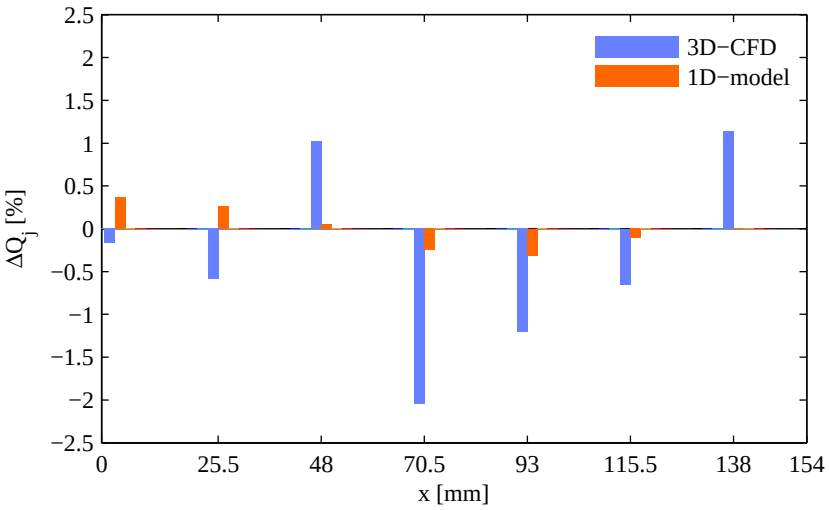

(b)

Figure 3.18.: Case A4f: (a) streamwise variation of the relative static pressure $\Delta p = p - p_0$; (b) relative outflow rate ΔQ_j at the individual exits $j = 1 \ldots 7$ (counted from left).

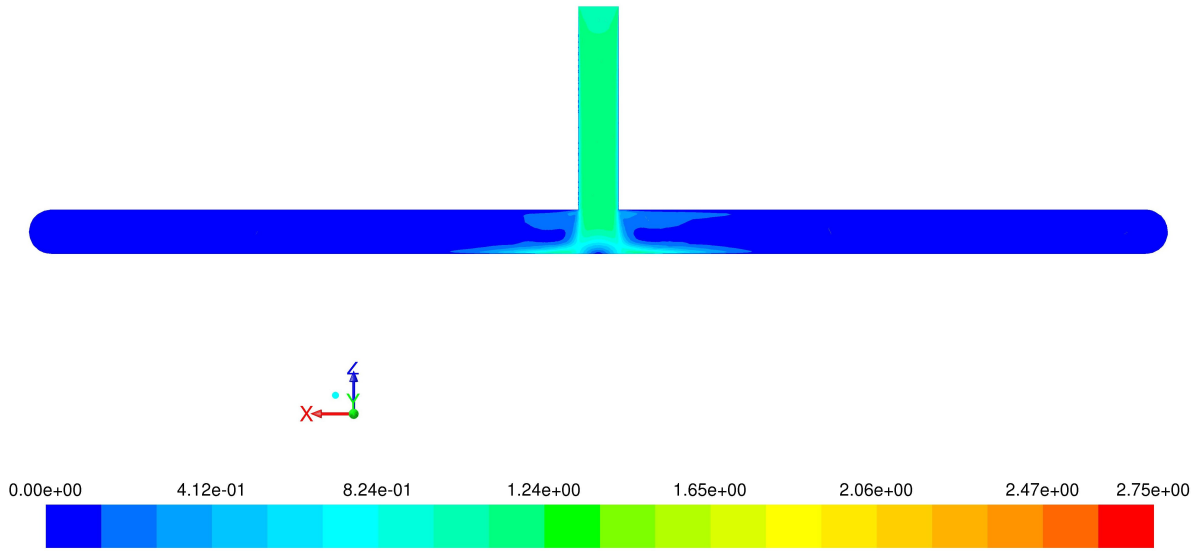

Figure 3.19.: Case A3f: contours of velocity magnitude in $\mathrm{m\,s^{-1}}$ on a horizontal cutting plane at $y = 10$ obtained from the CFD simulations.

Case	*We*						
	1	2	3	4	5	6	7
A1f	9.4	9.3	9.7	9.1	9.1	9.3	9.7
A2f	37.8	37.4	38.7	36.3	35.9	37.4	38.8
A3f	85.4	84.5	87.6	83.2	84.2	84.5	87.4
A4f	150.5	149.2	154.1	144.8	147.4	149.0	154.5

Table 3.5.: Cases A1f–A4f: jet exit Weber numbers *We* at the orifices 1–7 obtained from the CFD results.

3.2.4. One-dimensional model with modified parameter setting based on 3D-CFD results

The results of the one-dimensional approach presented so far always assume a unity momentum recovery factor $K = 1$, and the values listed in table 3.2 for the discharge coefficient C, which have been obtained from separate CFD simulations of axisymmetric flow from a reservoir through one single exit hole. The assumption of these values shall be validated against their counterparts extracted from the results of the three-dimensional CFD calculations for all cases A1–A4.

The values of the discharge coefficient which are extracted from the three-dimensional CFD results for all three different inlet positions (top, left, and front) at the investigated flow rates are listed in table 3.6. It can be seen that the discharge coefficients do not vary much from hole to hole, so that the assumption of a uniform discharge coefficient for all exit holes appears to be justified. On the other hand, the shown values lie generally somewhat below the corresponding values used in the one-dimensional model listed in table 3.2. This explains the fact that the mean level of the static pressure inside the dispenser observed in the one-dimensional results is always lower than the corresponding level seen in the three-dimensional CFD results. The

Case	Discharge coefficient C						
	1	2	3	4	5	6	7
A1t	0.77	0.76	0.79	0.80	0.77	0.77	0.78
A2t	0.80	0.79	0.82	0.82	0.80	0.79	0.81
A3t	0.81	0.81	0.83	0.85	0.81	0.81	0.82
A4t	0.82	0.83	0.85	0.86	0.83	0.83	0.84
A1l	0.76	0.80	0.80	0.77	0.76	0.76	0.78
A2l	0.79	0.82	0.81	0.81	0.79	0.79	0.81
A3l	0.76	0.77	0.78	0.76	0.76	0.77	0.78
A4l	0.77	0.78	0.79	0.77	0.77	0.78	0.79
A1f	0.77	0.77	0.78	0.76	0.76	0.77	0.78
A2f	0.80	0.79	0.81	0.79	0.78	0.79	0.81
A3f	0.81	0.80	0.82	0.80	0.80	0.80	0.82
A4f	0.82	0.82	0.83	0.81	0.81	0.82	0.83

Table 3.6.: Cases A1–A4: discharge coefficient obtained from the three-dimensional CFD results.

increase of C with increasing flow rates is observed in the values extracted from the three-dimensional CFD results as well.

The values for the momentum recovery factor K extracted from the three-dimensional CFD simulations of the 7-hole dispenser are listed in table 3.7. As discussed in section 2.1.2, K has theoretically to be within a range from 0 to 1. Some of the values for K determined from the CFD results are outside this interval and therefore discarded in table 3.7. This mainly affects the values of K for the holes number 1 and 4 in all cases with inlet on the top plane, A1t–A4t, and hole number 1 in all cases with the inlet located on the left side of the dispenser body, A1l–A4l. Near these holes the complex three-dimensional structure of the flow leads to pressure gradients, which predominate over the change in the static pressure expected at the outlet ports, which is caused by the loss of the axial momentum carried by the portion of liquid exiting the dispenser. This is evidently the case for A1t–A4t with the inlet on the top plane of the dispenser, where the jet like inflow impinges on the orifice plate closely downstream of hole number 4 as exemplarily shown in figure 3.9 for case A3t. This leads to a stagnation point next to the hole number 4 with a local maximum in static pressure resulting in a high pressure gradient into the streamwise direction. This gradient prevails over the expected pressure rise due to the branching-off of fluid through the exit port. The conditions which lead to unrealistic values of K at outlet number 1 for the cases A1t–A4t can be exemplarily seen in figure 3.9 for case A3t. Not the hole amount of fluid reaching the cross-section upstream outlet number 1 leaves the dispenser through this exit port. A portion of the fluid remains inside and gets redirected at the closed end of the dispenser, leading to a reverse flow. This redirection of the flow at the closed end, downstream of outlet number 1, causes a stronger increase of the static pressure there as it would be the case, when all oncoming liquid would exit the dispenser through the hole number 1. As seen from figure 3.14 the region near the horizontal inlet in the cases A1l–A4l exhibits as well considerable reverse flow near the hole number one, which finally leads to values of K outside the allowed range.

The configuration with the inlet on the left side of the dispenser body, represented by the cases A1l–A4l, yielded the best agreement between the results of the one-dimensional model

Case	Momentum recovery factor K						
	1	2	3	4	5	6	7
A1t	–	0.58	1.00	–	0.35	0.26	0.50
A2t	–	0.57	0.03	–	0.21	–	–
A3t	–	0.39	0.33	–	0.27	0.39	0.64
A4t	–	0.38	0.31	–	0.25	0.37	0.66
A1l	–	0.69	0.90	0.08	0.67	–	0.74
A2l	–	0.77	–	0.41	0.89	0.71	–
A3l	–	0.23	0.56	0.64	0.57	0.50	0.36
A4l	–	0.22	0.52	0.61	0.57	0.51	0.39
A1f	0.48	0.34	0.32	0.07	0.59	0.63	0.42
A2f	0.47	0.39	0.50	–	0.47	0.61	0.19
A3f	0.35	0.33	0.35	0.52	0.53	0.40	0.22
A4f	0.34	0.31	0.35	0.54	0.56	0.40	0.19

Table 3.7.: Cases A1–A4: momentum recovery factors obtained from the three-dimensional CFD results.

and the three-dimensional CFD, as it has been shown in the variations of the static pressure and outflow rate in figures 3.10 to 3.13. This can be attributed to the fact that with the inlet on the left side the three-dimensional flow phenomena associated with the jet-like inflow affect only a comparatively limited region near the inlet. Thus, in the larger remaining part further downstream the flow conditions are fairly close to the one-dimensional approximation. This particular inlet configuration is reconsidered to exemplarily show for the case A3l the potential to further improve the predictions of the one-dimensional model by using the discharge coefficients and the momentum recovery factors extracted from the three-dimensional results at each exit hole. Figure 3.20 shows the results for the variation of the static pressure and the outflow rate computed from the one-dimensional model using the modified parameter settings for C and K compared against the corresponding results of the three-dimensional CFD. Except for the region near the inlet at the left hand side, where the flow is strongly affected by three-dimensional effects, the agreement in the pressure profiles is markedly improved in comparison to the results obtained with the original parameter setting shown in figure 3.12. The improved agreement is also clearly seen in the prediction for the outflow distribution by comparing figure 3.20b against 3.12b.

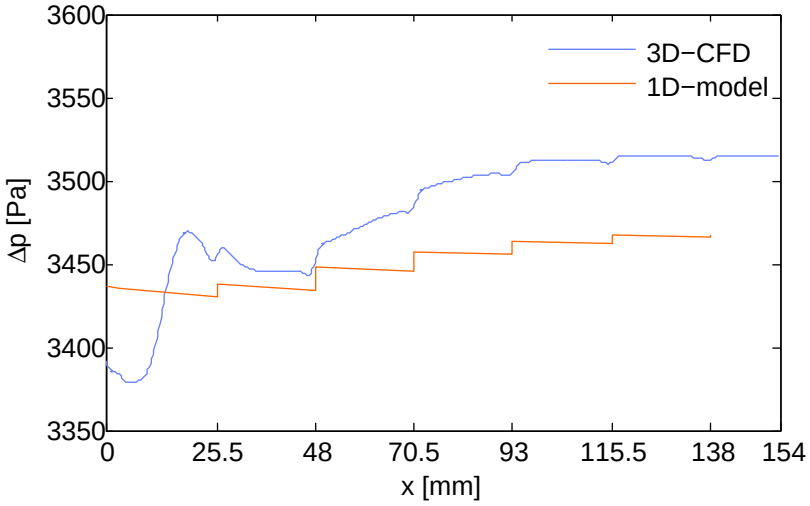

(a)

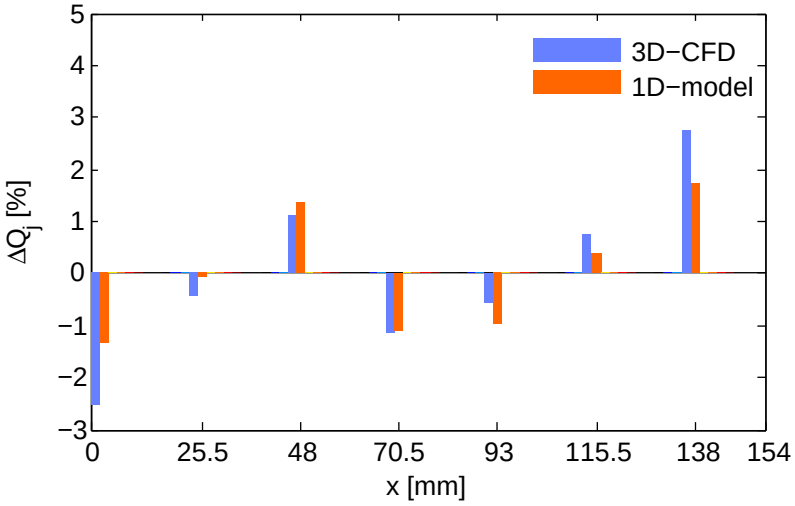

(b)

Figure 3.20.: Case A3l: (a) stream-wise variation of the relative static pressure $\Delta p = p - p_0$; (b) relative outflow rate ΔQ_j at the individual exits $j = 1 \ldots 7$ (counted from left); Parameter setting for discharge coefficient C and recovery factor K based on three-dimensional CFD results.

3.3. Type B: Slot dispenser

The dispenser type B has the same body as type A, described in section 3.2. Instead of the 7-hole plate used for the type A dispenser, dispenser type B is equipped with a narrow slot plate of the same thickness as the 7-hole plate. The slot has a length $l_{\text{slot}} = 120\,\text{mm}$ and a width $b_{\text{slot}} = 0.1\,\text{mm}$. The dispenser type B was computed only with the one-dimensional approach assuming always the inlet on the left hand side of the dispenser body. The flow domain is illustrated in figure 3.21. The working fluid, the investigated flow rates at the inlet boundary and the outlet boundary conditions are the same as for the type A dispenser, discussed in section 3.2. All considered cases for the dispenser type B are summarized in table 3.8.

The discharge coefficient required as input to the one-dimensional approach was obtained from a two-dimensional CFD simulation of the outflow from a reservoir through a narrow slot. The computational domain used for this CFD simulation is shown in figure 3.22. The reservoir has a rectangular cross section of $b_{\text{reservoir}} = 6\,\text{mm}$ width, and 10 mm height. Both the reservoir and the slot are assumed to be of infinite length into the x-direction, so that the flow is planar allowing for a two-dimensional simulation. The inlet is located at the upper boundary of the reservoir. A uniform normal inlet velocity v_{in} is imposed as boundary condition here. Its value is determined from the volumetric flow rates in the considered cases B1–B4 (see table 3.8) and the cross-sectional area of the slot written as

$$v_{\text{in}} = \frac{Q}{l_{\text{slot}} b_{\text{reservoir}}}.$$

A pressure-outlet boundary condition is imposed at the exit cross-section of the slot, prescribing a gauge pressure of 0 Pa. For the considered cases B1–B4 the simulated flow from the reservoir through the slot can be assumed as laminar. Based on the results of the CFD simulation the discharge coefficient for the slot was calculated according to equation (2.17). The values of the discharge coefficient obtained for all cases B1–B4 are listed in table 3.9. They were further used as inputs into the one-dimensional computations of the flow through the considered dispenser type.

3.3.1. Cases B1–B4: Inlet on the left side

The streamwise variations of the static pressure produced by the one-dimensional computation shown in subfigures 3.23a–3.26a are essentially determined by the counterplaying effects of the pressure rise due to fluid branching-off and the pressure loss due to frictional forces in the dispenser channel. In all cases B1–B4 the static pressure is increased from the inlet on the left hand side to the end of the channel on the right hand side, which implies that the effect of pressure rise dominates over frictional pressure loss. The variation of the outflow along the

Q $\text{ml}\,\text{min}^{-1}$	Type B: Slot plate
500	B1
1000	B2
1500	B3
2000	B4

Table 3.8.: Dispenser type B: considered test cases

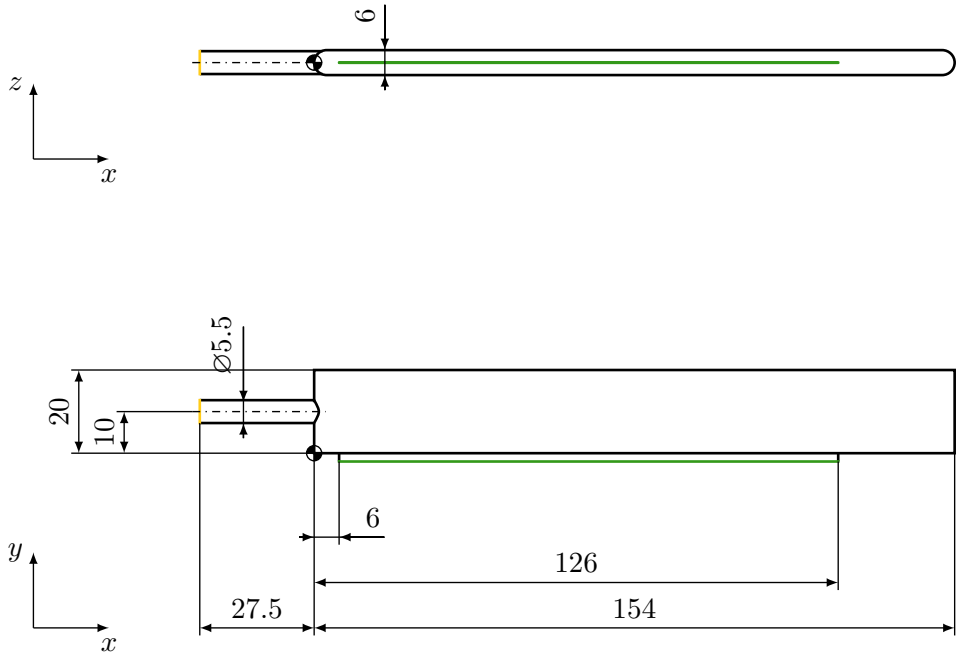

Figure 3.21.: Flow domain for dispenser type B (– inlet, – outlet).

Case	C
B1	0.34
B2	0.44
B3	0.49
B4	0.53

Table 3.9.: Dispenser type B: discharge coefficient C for a single orifice obtained from the 2D-CFD.

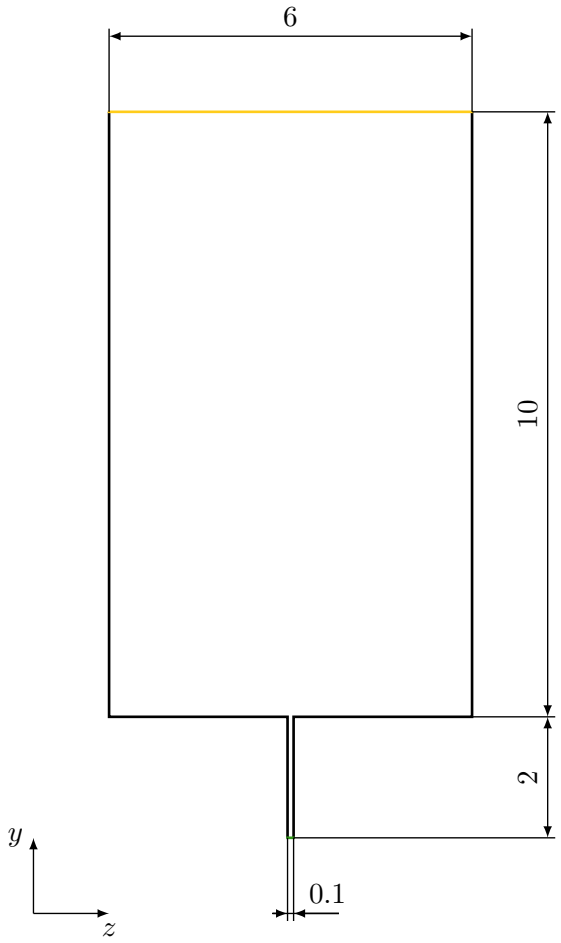

Figure 3.22.: Computational domain for the 2D-CFD calculation of the outflow from a reservoir through a slot infinitely extended into the x-direction. (– inlet, – outlet).

exit slot for each case is presented in subfigures 3.23b–3.26b in form of the deviation of the local outflow velocity $v(x)$ from a mean reference value $\bar{v}$ written as

$$\Delta v = \frac{v(x) - \bar{v}}{\bar{v}} \; 100 \; [\%].$$

The mean reference value reads

$$\bar{v} = \frac{Q}{A_{\text{slot}}}$$

with $A_{\text{slot}} = b_{\text{slot}} l_{\text{slot}}$ being the cross-sectional area of the slot. Analogously to the one-dimensional results for the dispenser type A with discrete exit holes, the variations of the relative outflow velocity for the continuous case with the exit slot follow exactly the trend of static pressure in the main channel, as it is laid down in the one-dimensional model formulation. The streamwise variations of the Weber number for the plane liquid exit jet based on the local exit velocity $v(x)$ and the slot width b_{slot} as characteristic velocity and length scales, respectively, are shown in the subfigures 3.23c–3.26c. The critical value required for a stable continuous outflow given by equation (2.37) is $We_{\text{crit}}^{\text{plane}} = 4$. Only in cases B3 and B4 the criterion for the formation of a stable jet is evidently met. In both cases the Weber numbers are still in a relatively low range (approximately 6 and 10.7), where a capillary breakup of the jets near downstream of the exit slot has to be expected. For the cases B1 and B2 the resulting Weber numbers are well below the critical value, so that the formation of a stable exiting planar jet is very unlikely in these cases.

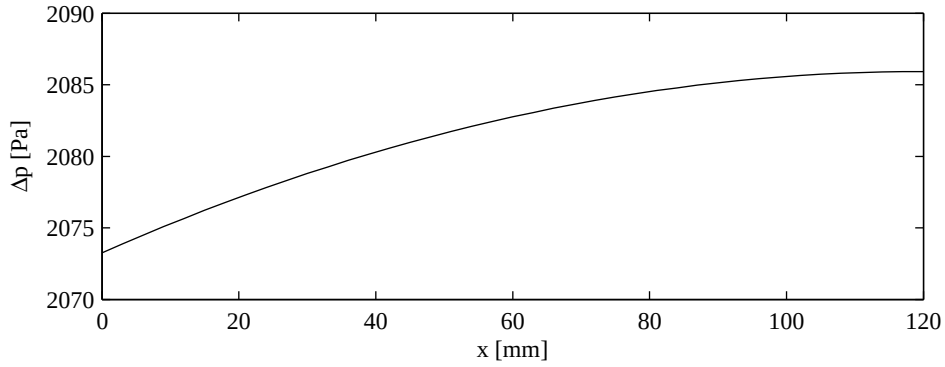

(a)

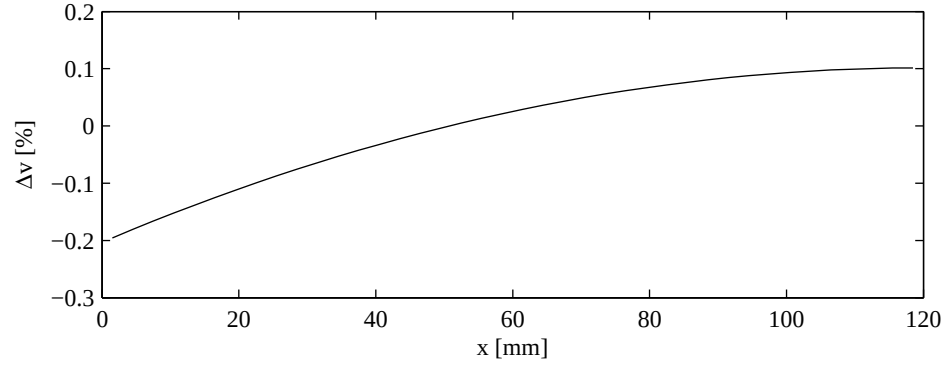

(b)

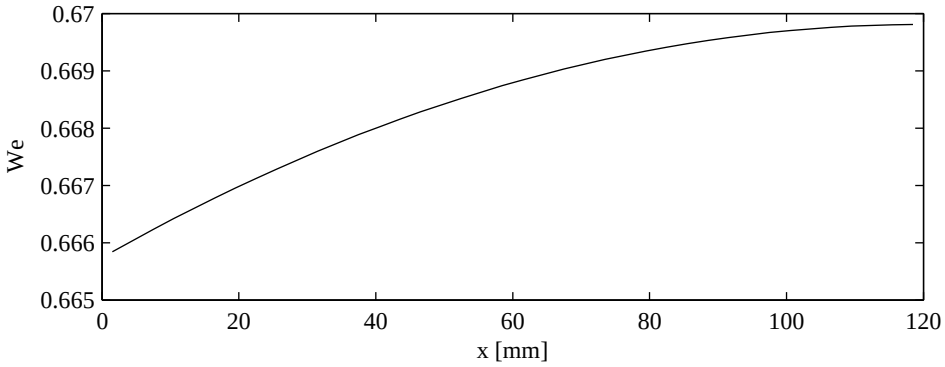

(c)

Figure 3.23.: Case B1: (a) relative pressure $\Delta p = p - p_0$, (b) relative outflow velocity $\Delta v = (v - \bar{v})/\bar{v}$ [%], and (c) Weber number We over the axial distance x.

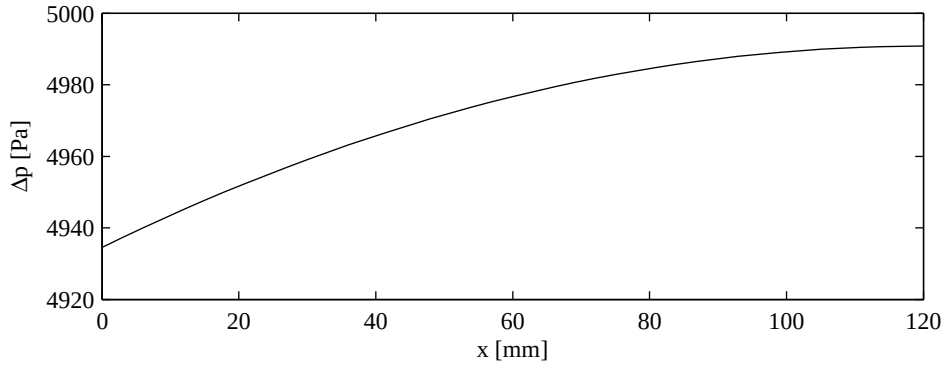

(a)

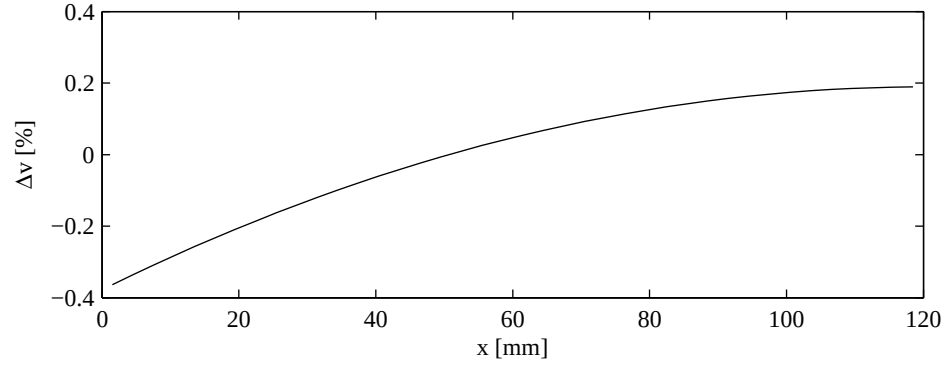

(b)

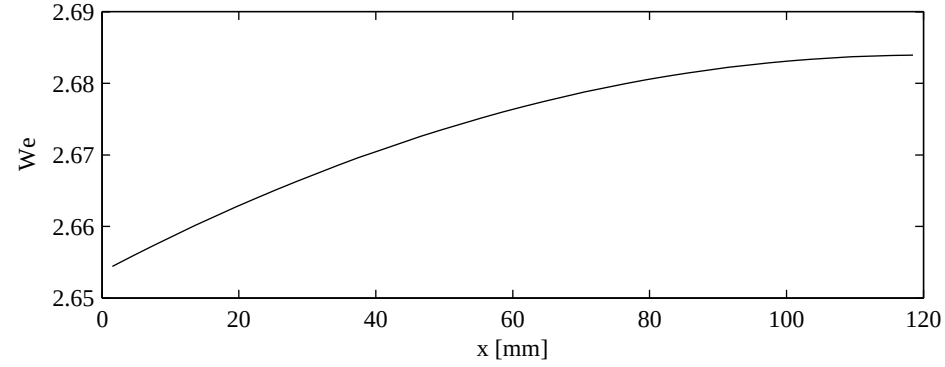

(c)

Figure 3.24.: Case B2: (a) relative pressure $\Delta p = p - p_0$, (b) relative outflow velocity $\Delta v = (v - \bar{v})/\bar{v}$ [%], and (c) Weber number We over the axial distance x.

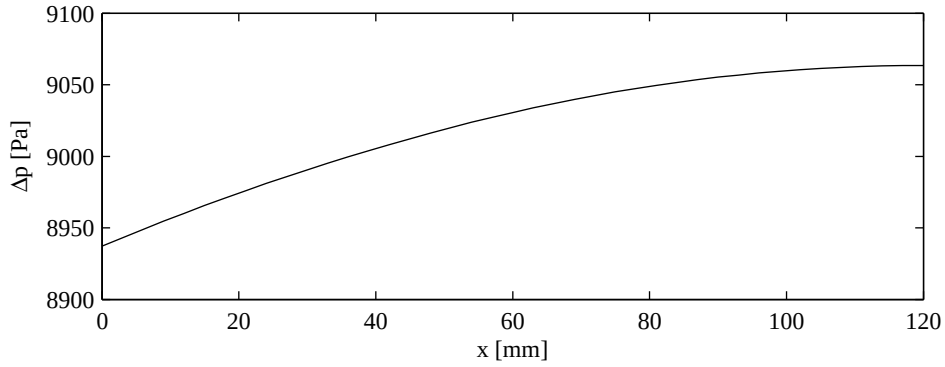

(a)

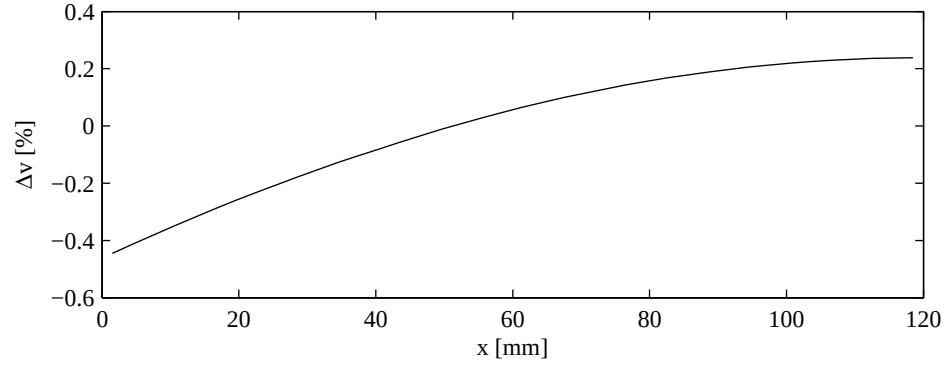

(b)

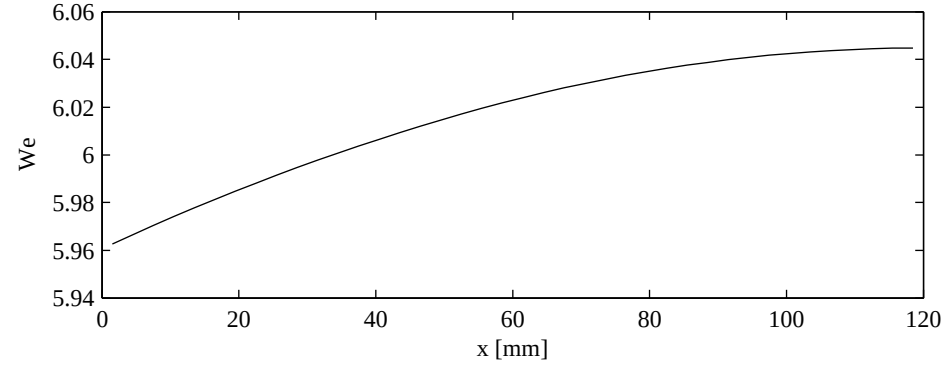

(c)

Figure 3.25.: Case B3: (a) relative pressure $\Delta p = p - p_0$, (b) relative outflow velocity $\Delta v = (v - \bar{v})/\bar{v}$ [%], and (c) Weber number We over the axial distance x.

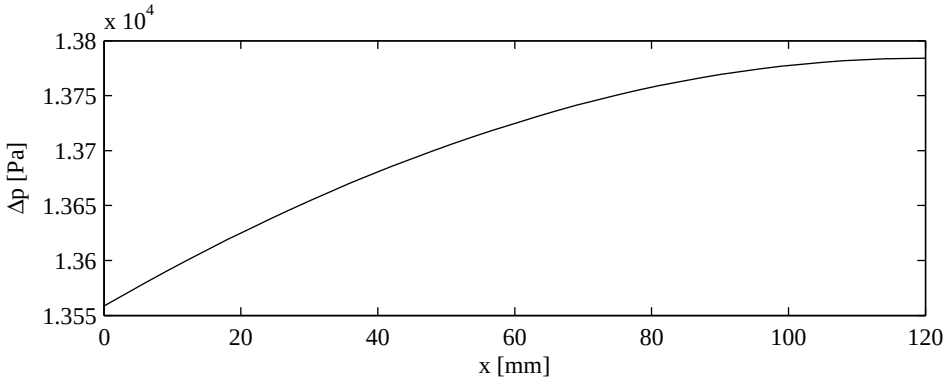

(a)

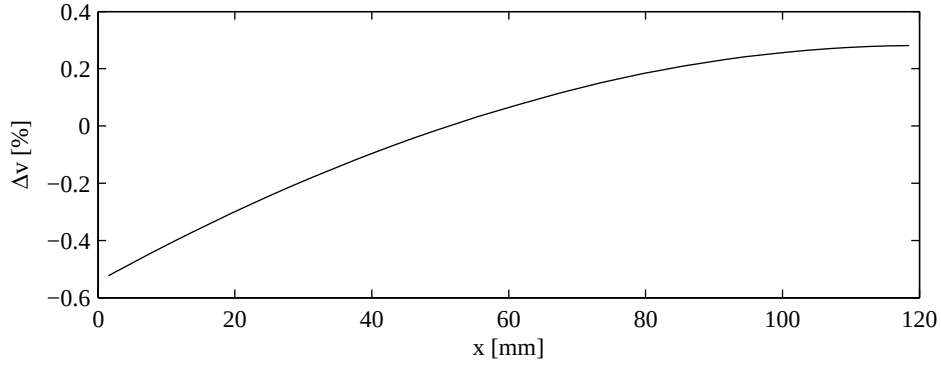

(b)

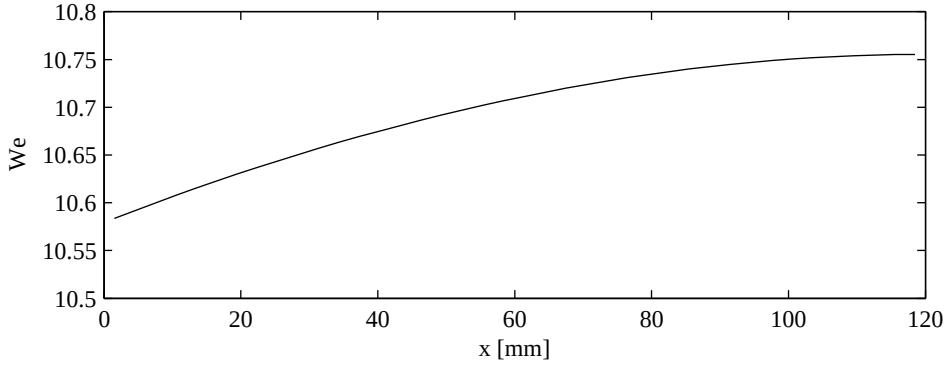

(c)

Figure 3.26.: Case B4: (a) relative pressure $\Delta p = p - p_0$, (b) relative outflow velocity $\Delta v = (v - \bar{v})/\bar{v}$ [%], and (c) Weber number We over the axial distance x.

3.3.2. Comparison of the results with the 7-hole dispenser

The results from the calculation of the slot dispenser for case B3 are compared to the corresponding results obtained from the one-dimensional model for the 7-hole dispenser for case A3l. In both cases the inlet is located at the left side as illustrated in figure 3.2. The volumetric flow rate at the inlet is the same for both cases. Figure 3.27 shows the cumulative outflow rate along the dispenser axis for both types of discharge. The step-like profile in figure 3.27 represents the cumulative outflow rate of the 7-hole dispenser, and the continuous profile the cumulative outflow rate of the slot dispenser. Beside the discrepancy caused by the discrete discharge in the one case and the continuous one in the other both dispenser type show similar outflow behavior near the ideal uniform distribution.

The continuous discharge from the slot dispenser evidently follows perfectly the ideal uniform outflow distribution. The discrete discharge through the seven-hole dispenser shows some deviation from the ideal uniform distribution at both ends of the dispenser. For the most part of the channel, it still comes very close to the ideal distribution.

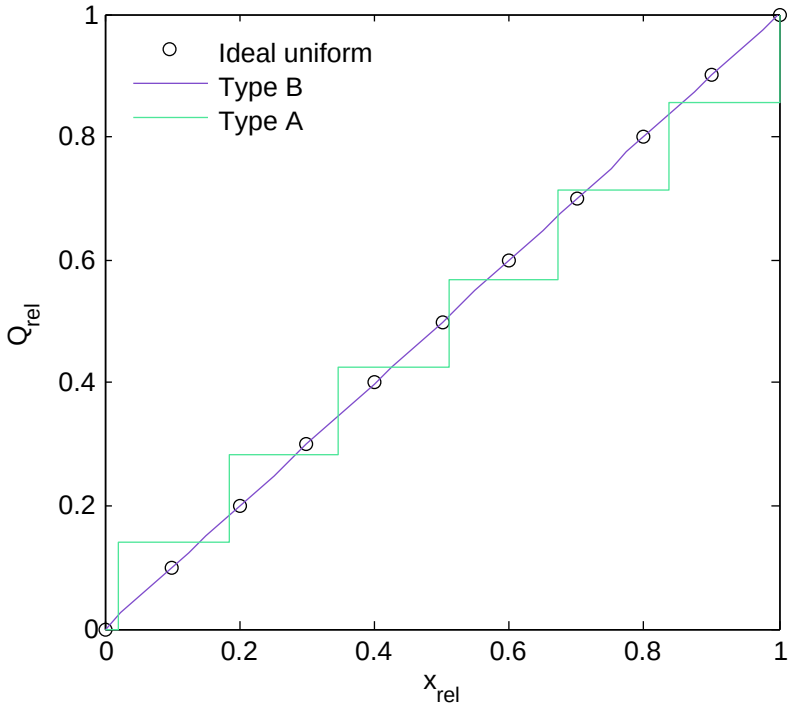

Figure 3.27.: Comparison of the cumulative outflow rates along the dispenser axis for a flow rate at the inlet of $1500\,\mathrm{ml\,min^{-1}}$ between the type B slot type dispenser (case B3) and the type A 7-hole dispenser (case A3l).

4. Summary and conclusions

The present work computationally investigated the flow through a multi-hole nozzle to lay the ground for a novel distributed dispense concept as an alternative to the presently used single-hole dispensers.

The computations were carried out using fully three-dimensional CFD-simulations as well as a well-established one-dimensional approach proposed in the literature for flows though manifolds. The obtained computational results lead to the following conclusions for the considered multi-hole and slot nozzle design:

- The gain in static pressure due to the successive branching-off of fluid through the exit ports generally overcompensates the losses in pressure due to frictional forces. This behavior is particularly seen in the results of the one-dimensional computations, where the level of the static pressure clearly shows an increasing tendency downstream from the position of the nozzle inlet port.

- For all considered inlet flow rates the investigated design produced fairly uniform distributions of the flow rates at the individual exits. The maximum deviation from the total-exit-area based average value is only 6%

- The seven-hole dispenser type and the slot dispenser type show both similar cumulative outflow rates along the dispenser axis. The slot dispenser follows almost exactly the ideal uniform distribution. The discrete dispense of the seven-hole nozzle deviates somewhat from the ideal distribution at both ends of the dispenser.

- Three-dimensional flow phenomena associated with the different alternatively considered nozzle inlet configurations have a quantitatively small but notable effect on the outflow rates through the individual exit holes. The effect manifests in a generally higher variation in the exit flow rates predicted by the three-dimensional CFD, as compared to the predictions of the one-dimensional approach, which by definition cannot account for any three-dimensional flow phenomena.

- The results of the one-dimensional model are shown to be significantly affected by the setting of the discharge coefficients at the individual exit holes. Setting these parameters to values which are extracted from the three-dimensional CFD results can significantly improve the predictions of the one-dimensional model. The influence of the momentum recovery factor on the computational results is comparatively small.

- The considered cases with the lowest inlet flow rate led to nozzle exit based Weber numbers, which come close to the critical lower limit for a transition from stable liquid jet flow to a discontinuous dripping. The occurrence of capillary breakup closely downstream of the exits has to be expected for these cases.

The numerical algorithm developed for the solution of the one-dimensional approach and programmed in Matlab was proven as a computationally very efficient tool for a first evaluation

of different multi-hole nozzle designs. A further version of this routine was extended to the case with a continuous distributed dispense, where the liquid leaves the nozzle through a long narrow exit slot.

A. Program descriptions

A.1. Manifold-1D: Discrete (multi-hole) dispense

The program Manifold-1D, consisting of the Matlab file "manifold_1d_2_1_0.m", calculates the outflow distribution of a blowing multi-hole dispenser with one or more branches based on the formulation for the multi-hole dispenser described in section 2.1.2. The calculation of the outflow rates is done iteratively going from cell $j = 1 \dots J_i$ for each branch $i = 1 \dots I$. The solution algorithm for a single cell is described in detail in section A.1.1. To fulfill the mass balance for each branch and over all branches, two iterative loops are introduced, which are described in detail in section A.1.2. Figures A.1 and A.2 illustrate the logical structure of the program.

A.1.1. Cell calculation algorithm

The static pressure and the velocity at the left face of cell j in branch i, $p_{i,j,\text{in}}$ and $u_{i,j}$, are known from the precursively done calculation of the cell on the left hand side. For the first cell of branch i, p_{in} and $u_{i,1}$ are guessed at the program start and subsequently recalculated until the mass balance is satisfied as described in section A.1.2. The unknowns of the current cell calculation are $u_{i,j+1}$, $v_{i,j}$, $p_{i,j+1,\text{in}}$ and $p_{i,j,\text{out}}$. $p_{i,j,\text{out}}$ can be calculated solely according to equation (2.12). $u_{i,j+1}$, $v_{i,j}$ and $p_{i,j+1,\text{in}}$ are described by the equations (2.15), (2.16) and (2.17), which can be combined to one single expression for $u_{i,j+1}$

$$u_{i,j+1} = \frac{-c_2 \pm \sqrt{c_2^2 - 4c_1c_3}}{2c_1}, \tag{A.1}$$

with c_1, c_2 and c_3 evaluated as:

$$c_1 = 1 + K_{i,j}C_{i,j}^2\alpha_{i,j}^2, \tag{A.2}$$

$$c_2 = -2u_{i,j}, \tag{A.3}$$

$$c_3 = \left(1 - K_{i,j}C_{i,j}^2\alpha_{i,j}^2\right)u_{i,j}^2 - \frac{2C_{i,j}^2\alpha_{i,j}^2}{\rho p_{i,j,\text{out}}}. \tag{A.4}$$

As stated by equation (A.1), there are two solutions for $u_{i,j+1}$. The first one represents the blowing and the second one the sucking manifold. This program focuses on the blowing case, where $u_{i,j+1}$ has to be smaller than $u_{i,j}$. Equation (A.1) can therefore be rewritten as

$$u_{i,j+1} = \frac{-c_2 - \sqrt{c_2^2 - 4c_1c_3}}{2c_1}. \tag{A.5}$$

With the solution for $u_{i,j+1}$ the remaining unknowns, $v_{i,j}$ and $p_{i,j+1,\text{in}}$, can be calculated:

$$v_{i,j} = \frac{1}{\alpha_{i,j}}\left(u_{i,j} - u_{i,j+1}\right), \tag{A.6}$$

$$p_{i,j+1,\text{in}} = p_{i,j,\text{out}} + K_{i,j}\rho\left(u_{i,j}^2 - u_{i,j+1}^2\right). \tag{A.7}$$

A.1.2. Iterative solution algorithm for the mass balances

The solution algorithm for the mass balances involves two different iterative loops. An inner loop n to satisfy the mass balance for a single branch, and an outer loop m to satisfy the total mass balance summed over all branches.

Within the inner loops the volumetric inflow rate into each branch is kept constant, and the inlet pressure is varied until the local mass balance for the branch is satisfied. The iteration method is derived from Bernoulli's equation for loss-free flow through the orifices. The motion of the fluid inside the dispenser body is thereby disregarded. The pressure at the inlet of branch i, $p_{i,1,\mathrm{in}}$, can then be approximated as a function of the actually obtained mean outflow velocity $\tilde{v}_i^{m,n}$

$$\tilde{p}_{i,1,\mathrm{in}}^{m,n} = \rho \frac{(\tilde{v}_i^{m,n})^2}{2}, \tag{A.8}$$

with

$$\tilde{v}_i^{m,n} = \frac{\sum_{j=1}^{J_i} Q_{i,j}^{m,n}}{\sum_{j=1}^{J_i} A_{i,j}}. \tag{A.9}$$

According to the mass balance for each branch i the mean outflow velocity can also be described as

$$\hat{v}_i^{m,n} = \frac{Q_i^m}{\sum_{j=1}^{J_i} A_{i,j}}, \tag{A.10}$$

which leads to another approximation for the inlet pressure

$$\hat{p}_{i,1,\mathrm{in}}^{m,n} = \rho \frac{(\hat{v}_i^{m,n})^2}{2}. \tag{A.11}$$

The volumetric flow rate error of branch i in the current step n, $\Delta Q_i^{m,n}$, can be written as

$$\Delta Q_i^{m,n} = Q_i^m - \sum_{j=1}^{J_i} Q_{i,j}^{m,n}.$$

Using equations (A.8)–(A.11) the difference $\Delta Q_i^{m,n}$ can now be transformed into a corresponding pressure difference $\Delta p_i^{m,n}$

$$\Delta p_i^{m,n} = \rho \frac{(Q_i^m)^2 - \left(\sum_{j=1}^{J_i} Q_{i,j}^{m,n}\right)^2}{2\left(\sum_{j=1}^{J_i} A_{i,j}\right)^2}. \tag{A.12}$$

Using this pressure difference the inlet pressure at each branch for the next step $n+1$ is computed as

$$p_{i,1,\mathrm{in}}^{m,n+1} = p_{i,1,\mathrm{in}}^{m,n} + \gamma_p \Delta p_i^{m,n}. \tag{A.13}$$

Due to the fact that $\Delta p_i^{m,n}$ is just an approximation the pressure correction must be underrelaxed by γ_p to ensure convergence. Test calculations turned out that a value of $\gamma_p = 0.7$ represents a good compromise between numerical stability and calculation speed.

Within each outer iteration loop m the flow rate at the inlet of each branch is varied to finally get a distribution of the inflow into all branches, where the static pressure at the inlet

of each branch is the same. To this end the inlet flow rate for each branch i after m outer steps is approximated using the equation

$$Q_i^m = v_i^m \sum_{j=1}^{J_i} A_{i,j}, \tag{A.14}$$

where v_i^m is computed dependent on the inlet pressure according to Bernoulli's equation for loss-free flow

$$v_i^m = \sqrt{\frac{2}{\rho} p_{\mathrm{in},i,1}^m}. \tag{A.15}$$

The target of the outer iterative loop is a uniform inlet pressure for all branches. For each outer step m this value is approximated by the arithmetic mean of the values of the static pressure actually obtained at each branch inlet $\bar{p}_{\mathrm{in},1}^m$

$$\bar{p}_{\mathrm{in},1}^m = \frac{\sum_{i=1}^{I} p_{\mathrm{in},i,1}^m}{I}.$$

This arithmetic mean pressure is used to approximate a corresponding inlet flow rate for each branch i written as

$$\bar{Q}_i^m = \bar{v}_i^m \sum_{j=1}^{J_i} A_{i,j}, \tag{A.16}$$

where the mean inlet velocity is obtained from the Bernoulli equation

$$\bar{v}_i^m = \sqrt{\frac{2}{\rho} \bar{p}_{\mathrm{in},1}^m}. \tag{A.17}$$

The deviation of the static pressure at each branch inlet from the targeted uniform value can be written as

$$\Delta p_i^m = \bar{p}_{\mathrm{in},1}^m - p_{\mathrm{in},1}^m$$

Using equations (A.14)–(A.17) the deviation Δp_i^m is transformed into a correction for the inlet flow rate for each branch i

$$\Delta Q_i^m = \sqrt{\frac{2}{\rho}} \sum_{j=1}^{J_i} A_{i,j} \left(\sqrt{\bar{p}_{\mathrm{in},1}^m} - \sqrt{p_{\mathrm{in},i,1}^m} \right) \tag{A.18}$$

The corrected inlet flow rates at each branch i for the next outer step $m+1$ are obtained as

$$Q_{i,1}^{m+1} = Q_{i,1}^m + \gamma_Q \Delta Q_i^m. \tag{A.19}$$

Due to the fact that ΔQ_i^m is just an approximation, the flow rate correction must be underrelaxed by γ_Q to ensure convergence. Test calculations revealed that a value of $\gamma_Q = 0.5$ represents a good compromise between numerical stability and calculation speed. The sum of the corrected inlet flow rates $Q_{i,1}^{m+1}$ over all branches $i = 1 \ldots I$ would not match the given total inflow rate. Therefore, the correction (A.19) is applied only to the branches $i = 1 \ldots I-1$. The inlet flow rate into the remaining branch is set to a value, so that the total inflow rate is satisfied.

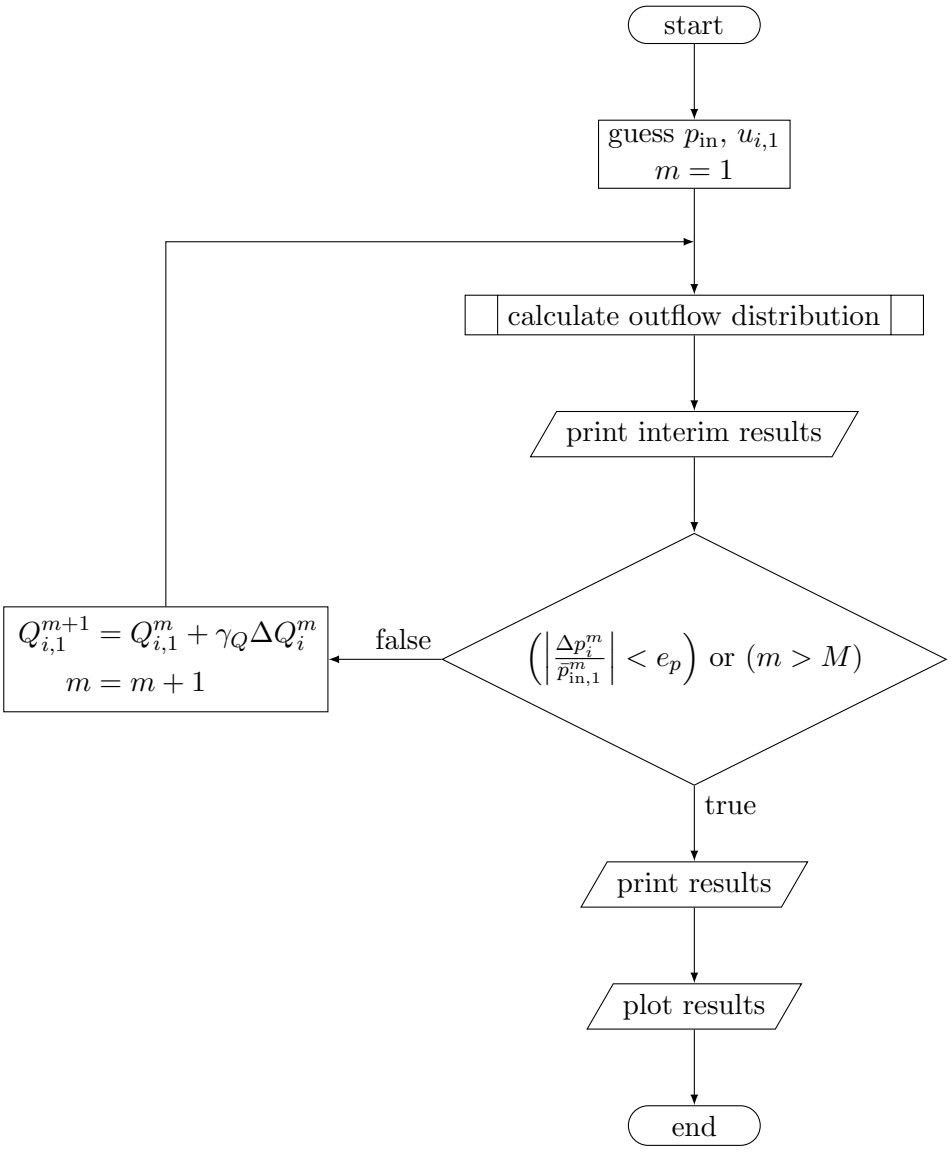

Figure A.1.: Main routine of Manifold-1d

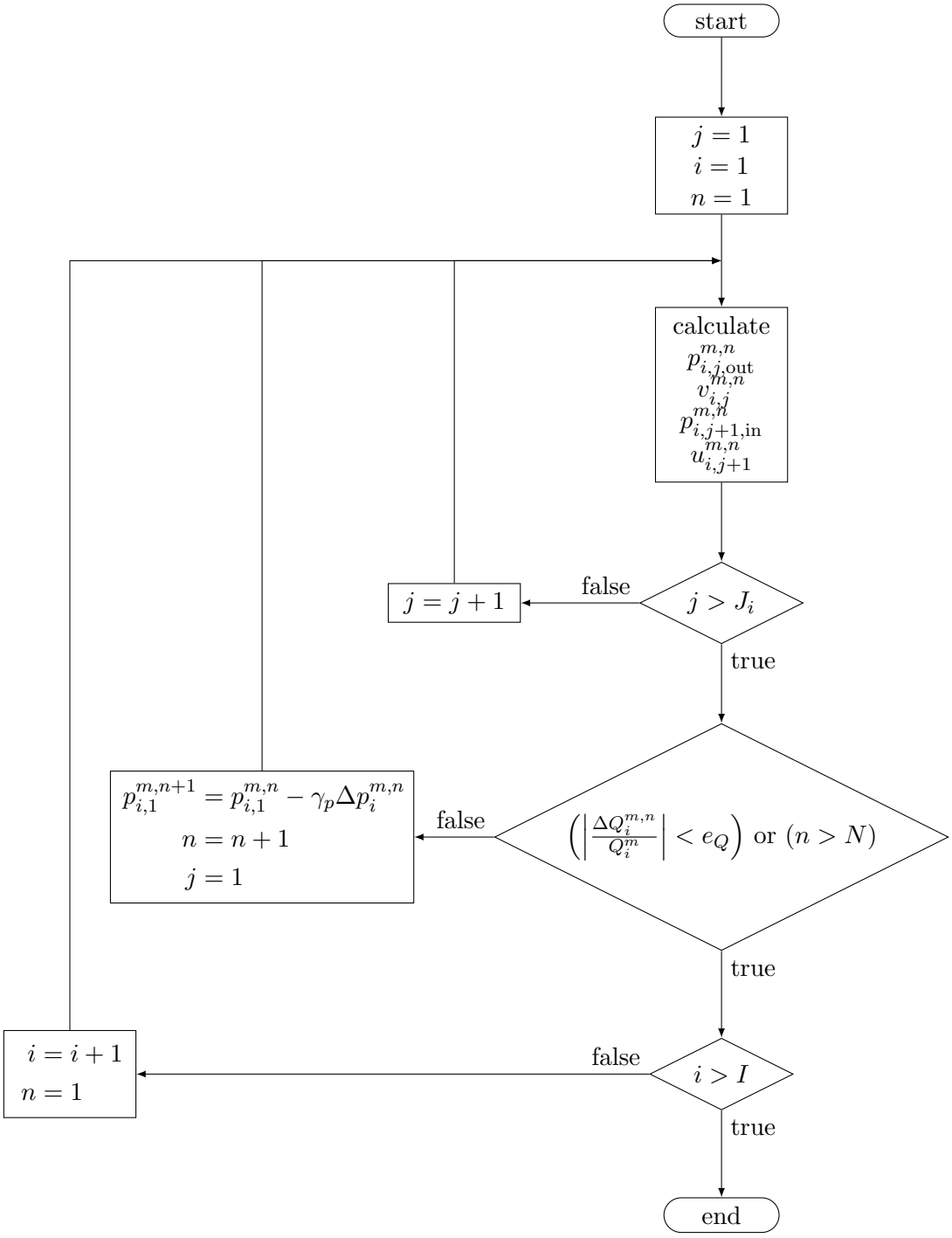

Figure A.2.: Manifold-1d subroutine “calculate outflow distribution”

A.2. Manifold-1D Continuous: Continuous (slot) dispense

The program Manifold-1D Continuous, consisting of the Matlab files "manifold_1d_ode_1_0.m" and "manifold_1d_continuous_1_0.m", calculates the outflow distribution of a continuously blowing dispenser based on the formulation described in section 2.1.2. The solution algorithm of the underlying equation system is described in section A.2.1. To fulfill the overall mass balance an iterative loop is introduced, which is described in detail in section A.2.2. Figure A.3 illustrates the logical structure of the program.

A.2.1. Differential equation solution algorithm

The behavior of the continuous dispenser is described by equations (2.24), (2.29) and (2.30) for the unknowns $u(x)$, $v(x)$ and $p(x)$. These three equations can be reduced to a system of two first-order differential equations by substituting $v(x)$ in (2.29) and (2.30) according to (2.24):

$$\frac{\mathrm{d}u}{\mathrm{d}x} = -\frac{bC}{A}\sqrt{\frac{2}{\rho}p(x)} \tag{A.20}$$

$$\frac{\mathrm{d}p}{\mathrm{d}x} = \frac{KbC}{A}u(x)\sqrt{8\rho p(x)} - \frac{\rho}{2}\zeta(u(x))u^2(x) \tag{A.21}$$

Equations (A.20) and (A.21) are solved numerically using an explicit Runge-Kutta formula derived by Dormand and Prince [2]. The initial value for $u(x)$, $u|_{x=0}$, is given by the prescribed volumetric flow rate at the dispenser inlet. The initial value for $p(x)$, $p|_{x=0}$, is guessed at the program start and subsequently adjusted until the overall mass balance is satisfied as described in section A.2.2.

A.2.2. Iterative solution for the mass balance

The solution algorithm involves a loop to compute the mass in balance. The mass balance at step m can be written as:

$$Q = \int_0^l v^m(x) b \mathrm{d}x + Q_{\mathrm{E}}^m. \tag{A.22}$$

Q_{E}^m in equation (A.22) is the error in the global volumetric flow rate. The inlet volumetric flow rate Q is prescribed. Disregarding the motion of fluid in the dispenser the outflow $\int_0^l v^m(x) b \mathrm{d}x$ is a function of the static pressure at the inlet $p|_{x=0}$, according to equation (2.17). To eliminate the error in the volumetric flow rate, the inlet pressure is corrected for the next step $m+1$:

$$p^{m+1}\big|_{x=0} = p^m|_{x=0} + \Delta p^m|_{x=0}\,. \tag{A.23}$$

According to Bernoulli's equation, the pressure correction $\Delta p^m|_{x=0}$ can be expressed by the difference between the targeted mean outflow velocity $\frac{Q}{\int_0^l b \mathrm{d}x}$ and the current mean outflow velocity $\frac{\int_0^l v^m(x) b \mathrm{d}x}{\int_0^l b \mathrm{d}x}$:

$$\Delta p^m|_{x=0} = \frac{\rho}{2\left(\int_0^l b \mathrm{d}x\right)^2}\left[Q^2 - \left(\int_0^l v^m(x) b \mathrm{d}x\right)^2\right]. \tag{A.24}$$

Substituting $\Delta p^m|_{x=0}$ into equation (A.23) by (A.24) finally allows to calculate the inlet pressure for the next step $p^{m+1}\big|_{x=0}$.

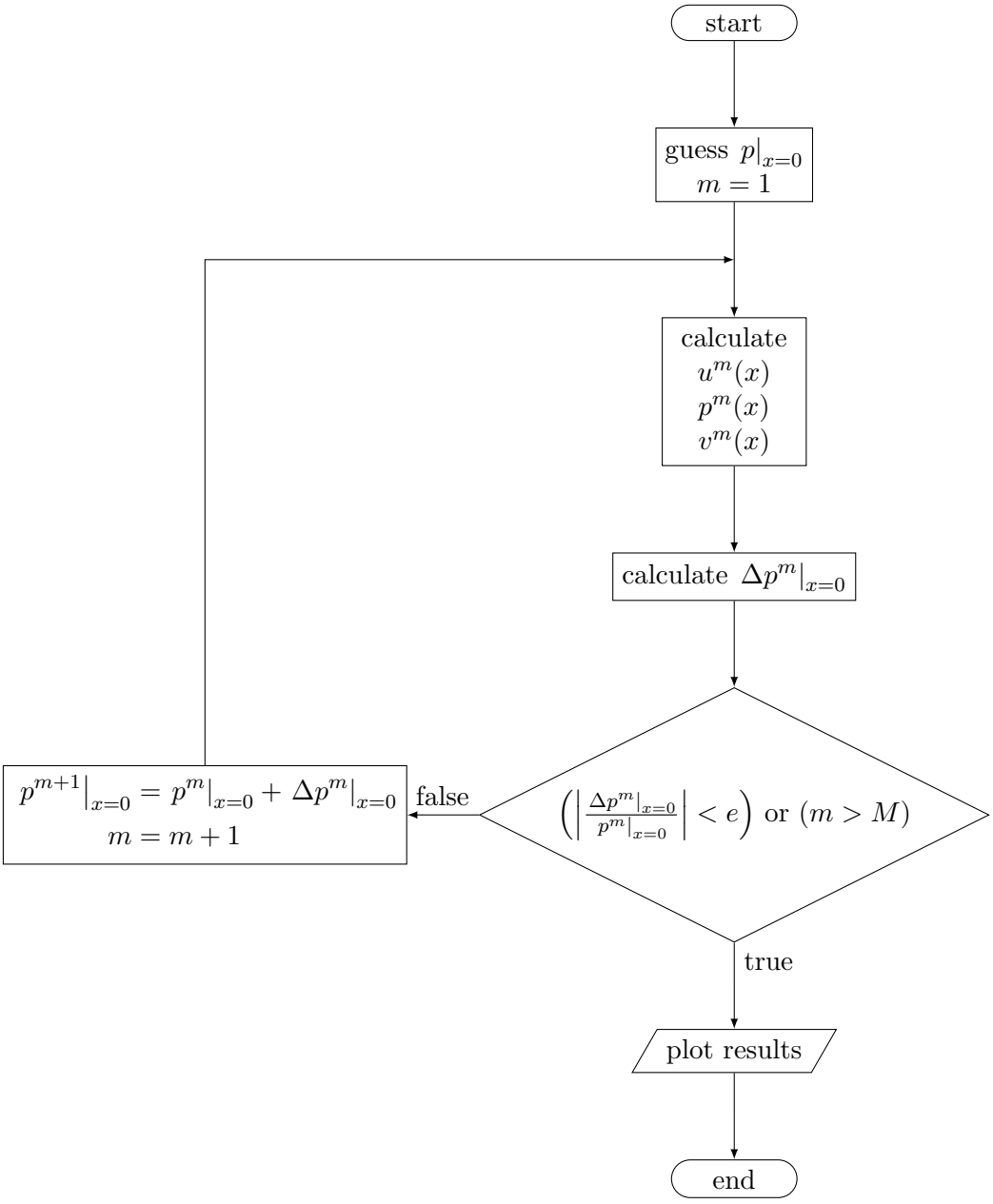

Figure A.3.: Main routine of Manifold-1d Continuous

Nomenclature

A	Cross-sectional area in m^2
b	Slot width in m
C	Discharge coefficient
D	Hydraulic diameter in m
d	Diameter in m
E	Energy in J
e	Maximum relative error
f	Fanning friction factor
g	Gravitational acceleration in $\mathrm{m\,s}^{-2}$
h	Slot height in m
I	Number of branches
i	Branch counter
J	Number of cells
j	Cell counter
K	Momentum recovery factor
k	Turbulent kinetic energy in $\mathrm{m}^2\,\mathrm{s}^{-2}$
l	Length in m
M	Maximum number of outer iterations
m	Outer iteration counter
N	Maximum number of inner iterations
n	Inner iteration counter
Oh	Ohnesorge number
P	Dimensionless static pressure
p	Static pressure in Pa

Q	Volumetric flow rate at the inlet in $\mathrm{m^3\,s^{-1}}$
r	Radial distance in m
Re	Reynolds number
S	Wetted perimeter in m
T	Pitch in m
U	Dimensionless velocity
u	Axial velocity component in $\mathrm{m\,s^{-1}}$
v	Vertical velocity component in $\mathrm{m\,s^{-1}}$
We	Weber number
x	Cartesian coordinate in m
y	Cartesian coordinate in m
z	Cartesian coordinate in m
α	Fraction of the internal area of the dispenser which is occupied by the orifices
Γ	Model parameter
γ	Under-relaxation factor
ϵ	Turbulent kinetic energy dissipation rate in $\mathrm{m^2\,s^{-3}}$
ζ	Pressure loss coefficient
λ	Friction factor
μ	Viscosity in $\mathrm{Pa\,s}$
ν	Kinematic viscosity in $\mathrm{m\,s^{-2}}$
ρ	Density in $\mathrm{kg\,m^{-3}}$
σ	Surface tension in $\mathrm{N\,m^{-1}}$

Bibliography

[1] A. Acrivos, B. D. Babcock, and R. L. Pigford. Flow distribution in manifolds. *Chemical Engineering Science*, 10(1–2):112–124, April 1959.

[2] J. R. Dormand and P. J. Prince. A family of embedded Runge-Kutta formulae. *Journal of Computational and Applied Mathematics*, 6(1):19–26, March 1980.

[3] A. V. Kulkarni, S. Roy Swarnendu, and J. B. Joshi. Pressure and flow distribution in pipe and ring spargers: Experimental measurements and cfd simulation. *Chemical Engineering Journal*, 133(1–3):173–186, September 2007.

[4] N. R. Lindblad and Schneider J. M. Production of uniform-sized liquid droplets. *Journal of Scientific Instruments*, 42(8):635–638, August 1965.

[5] W. T. Pimbley and D. H. Rickenbach. Fillet size in a liquid jet. *Journal of Fluids Engineering*, 101(1):105–108, 1979.

[6] H. Schlichting and K. Gersten. *Grenzschicht-Theorie*. Springer, Berlin, 10 edition, 2006.

[7] V. E. Senecal. Fluid distribution in process equipement. *Fluid Mechanics in Chemical Engineering*, 49(6):993–997, June 1957.

[8] Joseph H. Spurk and Nuri Aksel. *Strömungslehre: Einführung in die Theorie der Strömungen*. Springer, Berlin, 8 edition, 2010.

[9] P. Walzel. Koaleszenz von Flüssigkeitsstrahlen an Brausen. *Chemie Ingenieur Technik*, 52(8):652–654, 1980.